

1 On the drivers of droplet variability in Alpine mixed-phase 2 clouds

3
4 Paraskevi Georgakaki¹, Aikaterini Bougiatioti², Jörg Wieder³, Claudia Mignani⁴, Fabiola
5 Ramelli³, Zamin A. Kanji³, Jan Henneberger³, Maxime Hervo⁵, Alexis Berne⁶, Ulrike
6 Lohmann³ and Athanasios Nenes^{1,7}

7 ¹Laboratory of Atmospheric Processes and their Impacts, School of Architecture, Civil & Environmental
8 Engineering, École Polytechnique Fédérale de Lausanne, Lausanne, CH-1015, Switzerland

9 ²Institute for Environmental Research & Sustainable Development, National Observatory of Athens, P. Penteli,
10 GR-15236, Greece

11 ³Department of Environmental Systems Science, Institute for Atmospheric and Climate Science, ETH Zurich,
12 Zurich, CH-8092, Switzerland

13 ⁴Department of Environmental Sciences, University of Basel, Basel, CH-4056, Switzerland

14 ⁵Federal Office of Meteorology and Climatology, MeteoSwiss, Payerne, CH-1530, Switzerland

15 ⁶Environmental Remote Sensing Laboratory, School of Architecture, Civil & Environmental Engineering, École
16 Polytechnique Fédérale de Lausanne, Lausanne, CH-1015, Switzerland

17 ⁷Center for Studies of Air Quality and Climate Change, Institute of Chemical Engineering Sciences, Foundation
18 for Research and Technology Hellas, Patras, GR-26504, Greece

19 Correspondence to: Athanasios Nenes (athanasios.nenes@epfl.ch).
20

21 Abstract

22 Droplet formation provides a direct microphysical link between aerosols and clouds (liquid or
23 mixed-phase), and its adequate description poses a major challenge for any atmospheric model.
24 Observations are critical for evaluating and constraining the process. Towards this, aerosol size
25 distributions, cloud condensation nuclei, hygroscopicity and lidar-derived vertical velocities
26 were observed in Alpine mixed-phase clouds during the Role of Aerosols and Clouds Enhanced
27 by Topography on Snow (RACLETS) field campaign in the Davos, Switzerland region during
28 February and March 2019. Data from the mountain-top site of Weissfluhjoch (WFJ) and the
29 valley site of Davos Wolfgang are studied. These observations are coupled with a state-of-the-
30 art droplet activation parameterization to investigate the aerosol-cloud droplet link in mixed-
31 phase clouds. The mean CCN-derived hygroscopicity parameter, κ , at WFJ ranges between
32 0.2-0.3, consistent with expectations for continental aerosol. κ tends to decrease with size,
33 possibly from an enrichment in organic material associated with the vertical transport of fresh
34 ultrafine particle emissions (likely from biomass burning) from the valley floor in Davos. The
35 parameterization provides droplet number that agrees with observations to within ~25%. We
36 also find that the susceptibility of droplet formation to aerosol concentration and vertical
37 velocity variations can be appropriately described as a function of the standard deviation of the
38 distribution of updraft velocities, σ_w , as the droplet number never exceeds a characteristic limit,
39 termed “limiting droplet number”, of $\sim 150\text{-}550\text{ cm}^{-3}$, which depends solely on σ_w . We also
40 show that high aerosol levels in the valley, most likely from anthropogenic activities, increase

41 cloud droplet number, reduce cloud supersaturation ($<0.1\%$) and shift the clouds to a state that
42 is less susceptible to aerosol and become very sensitive to vertical velocity variations. The
43 transition from aerosol to velocity-limited regime depends on the ratio of cloud droplet number
44 to the limiting droplet number, as droplet formation becomes velocity-limited when this ratio
45 exceeds 0.65. Under such conditions, droplet size tends to be minimal, reducing the likelihood
46 that large drops are present that would otherwise promote glaciation through rime splintering
47 and droplet shattering. Identifying regimes where droplet number variability is dominated by
48 dynamical – rather than aerosol – changes is key for interpreting and constraining when and
49 which types of aerosol effects on clouds are active.

50

51 **1. Introduction**

52 Orographic clouds, and the precipitation they generate, play a major role in Alpine weather and
53 climate (e.g., Roe, 2005; Grubisic and Billings, 2008; Saleeby et al., 2013; Vosper et al., 2013;
54 Lloyd et al., 2015). The formation and evolution of orographic clouds involves a rich set of
55 interactions at different spatial and temporal scales encompassing fluid dynamics, cloud
56 microphysics and orography (Roe, 2005; Rotunno and Houze, 2007). Atmospheric aerosol
57 particles modulate the microphysical characteristics of orographic clouds by serving as cloud
58 condensation nuclei (CCN) that form droplets, or ice nucleating particles (INPs) that form ice
59 crystals (e.g., Pruppacher and Klett, 1997; Muhlbauer and Lohmann, 2009; Zubler et al., 2011;
60 Saleeby et al., 2013).

61 Emissions of aerosol particles acting as CCN and INPs can affect the microphysical and
62 radiative properties of clouds with strong (but highly uncertain) effects on local and regional
63 climate (IPCC, 2013; Seinfeld et al., 2016). Aerosol interactions with orographic clouds are
64 subject to even larger uncertainties, owing in part to the complex flows generated by the
65 interaction of the large-scale flow with the mesoscale orographic lifting and condensation, and
66 complex anisotropic turbulent air motions that arise (Roe, 2005; Smith, 2006; Rotunno and
67 Houze, 2007). Most importantly, orographic clouds are often mixed-phase clouds (MPCs),
68 which are characterized by the simultaneous presence of supercooled liquid water droplets and
69 ice crystals (Lloyd et al., 2015; Farrington et al., 2016; Lohmann et al., 2016; Henneberg et al.,
70 2017). MPCs remain one of the least understood cloud types, due to the multiple and highly
71 nonlinear cloud microphysical pathways that can affect their properties and evolution. MPCs
72 tend to glaciate (i.e., transition to pure ice clouds) over time because of the Bergeron-Findeisen
73 process, which is the rapid growth of ice crystals at the expense of the evaporating cloud

74 droplets, owing to the higher saturation vapor pressure of liquid water over ice (Bergeron,
75 1935; Findeisen, 1938). Aerosol concentrations may also alter the microphysical pathways
76 active in MPCs and ultimately drive their glaciation state. For instance, increase in CCN
77 concentrations leads to more numerous and smaller cloud droplets, reducing the riming
78 efficiency of ice crystals and therefore the hydrometeor crystal mass and the amount of
79 precipitation (Lohmann and Feichter, 2005; Lance et al., 2011; Lohmann, 2017). This
80 mechanism counters the glaciation indirect effect, where increases in INP concentrations
81 elevate ice crystal number concentration (ICNC) and promotes the conversion of liquid water
82 to ice - therefore the amount of ice-phase precipitation (Lohmann, 2002). Increases in CCN
83 can also decrease cloud droplet radius, and impede cloud glaciation, owing to reductions in
84 secondary ice production (SIP), which includes rime splintering, collisional break-up and
85 droplet shattering (Field et al., 2017; Sotiropoulou et al., 2020, 2021).

86 Cloud-scale updraft velocity (i.e., the part of the vertical velocity spectrum with positive
87 values) is the major driver of droplet formation, owing to the supersaturation generated from
88 adiabatic expansion and cooling (e.g., Nenes et al., 2001; Ghan et al., 2011). Despite its
89 importance, the simulation of updraft velocity by atmospheric models is rarely constrained by
90 observations, which can lead to large uncertainties in climate and numerical weather prediction
91 models (Sullivan et al., 2016, 2018). Reutter et al. (2009) pointed out that droplet formation in
92 clouds can be limited by the amount of CCN present (called the “aerosol-limited” regime), or
93 by the vertical velocity that generates supersaturation in the cloudy updrafts (called the
94 “velocity-limited” regime). Over the complex Alpine terrain, vertical motions can be
95 significantly shaped by the effects of orography (Lohmann et al., 2016). Orographic MPCs
96 have been frequently observed in the Swiss Alps under high updraft velocity conditions, where
97 supersaturation with respect to liquid water is formed faster than it is depleted by diffusional
98 and collisional ice growth processes (Korolev and Isaac, 2003) leading to persistent MPCs
99 (Lohmann et al., 2016).

100 Given the importance of droplet number for the radiative cloud properties and
101 microphysical evolution of Alpine MPCs, it is essential to understand the main aerosol and
102 dynamics properties that drive droplet formation. A limited number of studies exist that discuss
103 this very important topic, focusing though on liquid-phase clouds (Hammer et al., 2014, 2015;
104 Hoyle et al., 2016). Hoyle et al. (2016) showed that 79% of the variance in droplet number in
105 warm clouds formed at the high-altitude ~~Swiss Alps research station of Jungfrauoch~~ station in
106 the Swiss Alps (3450 m a.s.l.) is driven by variations in potential CCN concentration (i.e.:
107 aerosol particles with a dry diameter >80 nm). ~~With box~~ Using a cloud parcel model

Formatted: French (Switzerland)

Field Code Changed

Formatted: French (Switzerland)

Field Code Changed

Field Code Changed

Formatted: French (Switzerland)

Formatted: French (Switzerland)

Field Code Changed

Formatted: French (Switzerland)

Formatted: French (Switzerland)

Formatted: French (Switzerland)

Formatted: French (Switzerland)

108 ~~simulations~~, Hammer et al. (2015) ~~also~~ investigated the influence of updraft velocity, particle
109 concentration and hygroscopicity on ~~droplet~~liquid cloud formation ~~in the Alpine region~~, and
110 found that variations in vertical wind velocity have the strongest influence on the aerosol
111 activation. ~~The ability~~Up to ~~predict~~now we are not aware of in-situ studies assessing cloud
112 droplet ~~number~~closure in MPCs, where the existence of ice crystals can deplete supersaturation
113 or the low temperatures may decrease CCN activity through the formation of glassy aerosol-
114 ~~has not been assessed in a closure study to date~~.

115 Here we analyze observational data collected as part of the Role of Aerosols and Clouds
116 Enhanced by Topography on Snow (RACLETS) field campaign, which was held in the region
117 of Davos, Switzerland, during February and March 2019. This intensive field campaign aims
118 to address questions related to the modulators of orographic precipitation, the drivers of the
119 enhanced ice-crystal number concentrations observed in MPCs as well as the human-caused
120 pollution effects on cloud microphysical and optical properties. Through this study we focus
121 on a two-week period seeking to unravel the complex aerosol-droplet-updraft velocity
122 interactions that occur in the orographic MPCs. For this, we combine CCN number
123 concentrations with the particle size distributions to understand the variations in hygroscopicity
124 over time and for sites located in the valley and a close by mountain-top site. The in-situ
125 measurements are subsequently coupled with a state-of-the art droplet parameterization to
126 determine the potential droplet numbers and the corresponding maximum supersaturation
127 achieved in cloudy updrafts. The predicted droplet numbers are evaluated against direct
128 observations, and the degree to which droplet formation is velocity- or aerosol-limited is
129 determined for the whole timeseries.

130

131 2. Methods

132 2.1 Observational datasets

133 ~~The~~This analysis utilizes measurements collected during the RACLETS campaign, which took
134 place from 8 February to 28 March 2019 ([https://www.envidat.ch/group/about/raclets-field-](https://www.envidat.ch/group/about/raclets-field-campaign)
135 [campaign](https://www.envidat.ch/group/about/raclets-field-campaign)) (Mignani et al., ~~2020~~2021; Ramelli et al., ~~2020b, c~~2021a, b; Lauber et al.,
136 ~~2020~~2021). This joint research project offers a unique dataset of orographic clouds,
137 precipitation and snow measurements in an effort to shed light on some fundamental
138 microphysical processes being present in subsequent stages of the lifecycle of clouds (i.e.,
139 cloud formation, precipitation onset, cloud dissipation). All measurements presented in this
140 paper were performed at two distinct observation stations near Davos, Switzerland (supplement

Formatted: French (Switzerland)

Formatted: French (Switzerland)

Formatted: French (Switzerland)

Formatted: French (Switzerland)

Formatted: French (Switzerland)

Formatted: French (Switzerland)

Formatted: French (Switzerland)

141 Fig. S1). A measurement site is located at Davos Wolfgang, which is the pass between Davos
142 (1560 m a.s.l.) in the South and Klosters (1200 m a.s.l.) in the North and is otherwise known
143 as Wolfgang-Pass (WOP; 1630 m a.s.l., 46°50'08.076"N 9°51'12.939"E). Measurements were
144 also conducted at the mountain-top station Weissfluhjoch (WFJ; 2700 m a.s.l., 46°49'58.670"N
145 9°48'23.309"E), which is located ~1 km above the valley floor in Davos, in the eastern part of
146 the Swiss Alps. The current study primarily focuses on data collected during a two-week period
147 of interest, which spans from 24 February to 8 March 2019. During the RACLETS campaign,
148 a defective sheath air filter affected the CCN measurements collected at WFJ, thus inhibiting
149 data usage from the instrument for a large duration of the campaign. Therefore, we limit our
150 analysis to the above-mentioned period, when the CCN counter was fully operational. Besides,
151 during the selected period two distinct weather patterns were observed (fair weather conditions
152 interrupted by a precipitating period), allowing for a contrasting analysis of the observed
153 scenarios. The following description refers to the measurements that provided the basis for the
154 present analysis (see Table 1).

155

156 2.1.1 Aerosol particle size distribution measurements

157 Particle size distributions were continuously monitored at WOP and WFJ using commercially
158 available Scanning Mobility Particle Sizers (SMPS; Model 3938, TSI Inc., US). At both
159 stations, the systems consisted of a differential mobility analyzer (Model 3081, TSI Inc., US),
160 a soft X-ray neutralizer (Model 3088, TSI Inc., US) and a water-based condensation particle
161 counter (Model 3787 at WOP, Model 3788 at WFJ, TSI Inc. US). Running the particle counters
162 in low flow mode (0.6 Lmin^{-1}), using a sheath flow of 5.4 Lmin^{-1} and applying a total scanning
163 time of 2 minutes (scan time: 97 s, retrace time: 3 s, purge time: 10 s), particle size distributions
164 between 11.5 nm and 469.8 nm diameter were monitored.

165

166 2.1.2 CCN measurements

167 A Droplet Measurement Technologies (DMT) single-column continuous-flow streamwise
168 thermal gradient chamber (CFSTGC; Roberts and Nenes, 2005) was used to carry out in-situ
169 measurements of CCN number concentrations for different supersaturations (SS). The
170 CFSTGC consists of a cylindrical flow tube with wetted walls, inside which SS is developed
171 by applying a linear streamwise temperature gradient between the column top and bottom.
172 Owing to the greater mass diffusivity of water vapor than the thermal diffusivity of air, a
173 constant and controlled SS is generated with a maximum at the centerline of the flow tube. The
174 SS is mainly dependent on the applied temperature gradient, flow rate and pressure (Roberts

Formatted: Not Highlight

175 and Nenes, 2005). An aerosol sample flow is introduced at the column centerline, and those
176 particles having a critical supersaturation lower than the instrument *SS* will activate to form
177 droplets and will afterward be counted and sized by an Optical Particle Counter (OPC) located
178 at the base of the CFSTGC column. The *SS* developed within the instrument responds linearly
179 to changes in pressure, since its operation relies on the difference between heat and mass
180 diffusivity. Calibration of the instrument, which determines the output supersaturation, was
181 performed by the manufacturer at ~800 mbar, while throughout the campaign the CFSTGC
182 was operating at a lower pressure ~735 mbar, therefore the *SS* reported by the instrument is
183 adjusted by a factor of $\frac{735}{800} = 0.92$, which accounts for the difference between the ambient and
184 the calibration pressure (Roberts and Nenes, 2005). CCN concentrations were measured at a
185 specific *SS* for approximately 10 minutes; the instrument was cycled between 6 discrete values
186 ranging from 0.09% to 0.74% supersaturations, producing a full spectrum every hour. Each 10-
187 minute segment of the raw CCN data are filtered to discount periods of transient operation
188 (during supersaturation changes), and whenever the room temperature housing the instrument
189 changed sufficiently to induce a reset in column temperature (the instrument control software
190 always sets the column temperature to be at least 1.5 degrees above the room temperature to
191 exclude spurious supersaturation generation in the column inlet). The CFSTGC was deployed
192 on the mountain-top site of WFJ with the intention of relating the CCN measurements directly
193 to the size distribution and total aerosol concentration data measured by the SMPS instrument
194 at the same station.

195

196 *2.1.3 Cloud microphysical measurements*

197 In-situ observations of the cloud microphysical properties were obtained with the tethered
198 balloon system HoloBalloon (Ramelli et al., [2020a,2020](#)). The main component of the
199 measurement platform is the holographic cloud imager HOLIMO 3B, which uses digital in-
200 line holography to image an ensemble of cloud particles in the size range from 6 μm to 2 mm
201 diameter in a three-dimensional detection volume. Note that particles smaller than 6 μm are
202 not detected by HOLIMO, which means that the droplet number concentration may be
203 underestimated. Based on a set of two-dimensional images, information about the particle
204 position, size and shape can be obtained. The detected particles can be classified as cloud
205 droplets and ice crystals using supervised machine learning (Fugal et al., 2009; Touloupas et
206 al., 2020). The differentiation between cloud droplets (circular) and ice crystals (non-circular)
207 is done for particles exceeding 25 μm diameter based on their shape (Henneberger et al., 2013).

208 From the classification, the phase-resolved size distribution, concentration and content can be
 209 derived (Henneberger et al., 2013; Ramelli et al., [2020a](#),[2020](#)). The HoloBalloon platform was
 210 flying at WOP and provided vertical profiles of the cloud properties within the lowest 300
 211 meters of the boundary layer (BL). The current analysis utilizes the cloud droplet number
 212 concentration and liquid water content (LWC) measurements. Note that the LWC is calculated
 213 based on the size distribution of the cloud droplets using a liquid water density (ρ_w) of 1000 kg
 214 m⁻³ and is therefore dominated by large cloud particles.

215

216 **Table 1.** Overview of data sources from the RACLETS campaign used for this study. Along
 217 with the observed parameters, the corresponding instrumentation, measurements range and
 218 time resolutions are listed.

Measured parameter	Measurement site	Instrument	Measurement range	Time resolution
Aerosol number size distribution	WOP/ WFJ	Scanning Mobility Particle Sizer	11.5 – 469.8 nm	2 min
CCN number concentration	WFJ	Continuous flow streamwise thermal gradient CCN counter	$SS = 0.09 - 0.74\%$	1 s
Cloud droplet number concentration and liquid water content	WOP	Holographic cloud imager HOLIMO	6 $\mu\text{m} - 2 \text{ mm}$	10 – 20 s
Precipitation	WOP/ WFJ	Parsivel disdrometer/ MeteoSwiss weather station	0.2 mm – 25 mm	30 s
Horizontal wind speed and direction	WOP/ WFJ	MeteoSwiss weather station	–	10-min averages
Profiles of vertical wind speed	WOP	Wind Doppler Lidar	200 m – 8100 m AGL	5 s max

219

220 2.1.4 Meteorological data

221 During the measurement period, meteorological parameters (e.g., pressure, temperature,
222 precipitation, horizontal wind speed and direction) were continuously monitored by the
223 permanent MeteoSwiss observation station at WFJ. Additionally, a weather station was
224 installed on the OceaNet container (Griesche et al., 2019) deployed at WOP, which also hosted
225 several remote sensing instruments (e.g., Cloud radar, Raman Lidar, Microwave radiometer)
226 and a Particle Size Velocity (Parsivel) disdrometer (Parsivel2, OTT HydroMet GmbH,
227 Germany; Tokay et al., 2014) to measure precipitation. As there was no wind sensor included
228 in the weather station on the OceaNet container, we utilized the horizontal wind speed and
229 direction measurements from the nearby MeteoSwiss station in Davos, assuming that they
230 provide a good proxy for the wind regime in the valley. Vertical wind speed profiles were
231 obtained with a wind Doppler Lidar (WindCube 100S, manufactured by Leosphere) at WOP.
232 Throughout the campaign the wind lidar measured from 200 m to 8100 m above ground level
233 (AGL) with high temporal (5 s max) and vertical resolution (50 m). The wind lidar operated
234 following the Doppler Beam Switching technique with an elevation of 75°. More information
235 about the remote sensing measurements can be found in Ramelli et al. (2020b,2021a).

236 2.2 Aerosol hygroscopicity

237 The aerosol hygroscopicity parameter, κ , encompasses the impact of particle chemical
238 composition on its subsaturated water uptake and CCN activity (Petters and Kreidenweis,
239 2007). Here, we determine κ similar to the approach of Moore et al. (2011), Jurányi et al.
240 (2011), Latham et al. (2013), Kalkavouras et al. (2019), Kacarab et al. (2020) and others, by
241 combining the CCN measurements with the SMPS aerosol size distribution data as follows.
242 For each SMPS scan, the particle size distribution is integrated backward starting from the bin
243 with the largest-size particles – which corresponds to CCN with the lowest critical
244 supersaturation, S_{cr} . We then successively add bins with smaller and smaller diameters, until
245 the aerosol number matches the CCN concentration observed for the same time period as the
246 SMPS scan. The particles in the smallest size bin, which we call *critical dry diameter*, D_{cr} ,
247 correspond to CCN with highest S_{cr} possible – being the instrument supersaturation, SS . From
248 D_{cr} and SS we determine κ from Köhler theory (Petters and Kreidenweis, 2007), assuming the
249 particle chemical composition is internally mixed:
250

$$\kappa = \frac{4A^3}{27D_{cr}^3SS^2} \quad (1)$$

Formatted: Not Highlight

251 where $A = \frac{4M_w\sigma}{RT\rho_w}$ is the Kelvin parameter, while in which M_w (kg mol⁻¹) is the molar mass of
252 water, σ (J m⁻²) is the surface tension of the solution droplet, R is the universal gas constant and
253 T (K) is the ambient temperature. Here we assume the surface tension of the solution droplet is
254 equal to that of pure water ($\sigma = \sigma_w$) by convention. The κ determined above represents the
255 composition of particles with diameter D_{cr} (large particles can have a different κ but still
256 activate given that their S_{cr} is lower than the prevailing SS in the CCN chamber). This means
257 that over the course of an hour, over which a full SS cycle is completed, κ is determined for a
258 range of D_{cr} , which in our case were in the range of 50-200 nm (Section 3.1). This size-resolved
259 κ information provides insights on the possible origin and chemical components of the aerosol,
260 which is important given that there is no other measurement available to constrain chemical
261 composition during RACLETS. From κ , we infer an equivalent organic mass fraction, ε_{org} ,
262 assuming that the aerosol is composed of an organic-inorganic mixture:

$$\varepsilon_{org} = \frac{(\kappa - \kappa_i)}{(\kappa_o - \kappa_i)} \quad (2)$$

263 where $\kappa_i = 0.6$ and $\kappa_o = 0.1$ are characteristic hygroscopicity values for the inorganic fraction
264 of aerosol (represented by ammonium sulphate), and organic aerosol, respectively (Petters and
265 Kreidenweis, 2007; Wang et al., 2008; Dusek et al., 2010). Note that these values for a
266 continental aerosol are supported by observations and analyses (e.g., Andreae and Rosenfeld,
267 2008; Rose et al., 2008; Pringle et al., 2010).

268

269 2.3 Cloud droplet number and cloud maximum supersaturation

270 Here we apply adiabatic cloud parcel theory to the observational datasets to determine the
271 maximum in-cloud supersaturation (S_{max}) and cloud droplet number (N_d) that would form over
272 both measurement sites throughout the observation period. Droplet calculations are carried out
273 with the physically based aerosol activation parameterization of Nenes and Seinfeld (2003),
274 with extensions introduced by Fountoukis and Nenes (2005), Barahona et al. (2010), and
275 Morales and Nenes (2014). Each N_d calculation requires knowledge of the observed pressure,
276 temperature, vertical winds, aerosol size distribution and hygroscopicity. For the WFJ site, all
277 data are available as described in the sections above. For the WOP site, CCN (hence
278 hygroscopicity) data are not available, so we carry out N_d calculations at two κ values, 0.1 and
279 0.25, which is the upper and the lower limit determined from the WFJ analysis (Section 3.1).

280 The ability to reproduce observed cloud droplet number concentrations (“Method evaluation
281 against direct observations”, Section 3.2.1) further supports the selection of these values.

282 The wind lidar measurements conducted at WOP (Section 2.1.4) are used to determine
283 the prevailing vertical velocities at both sites. Data extracted from the first bin of the lidar,
284 being 200 m AGL, are considered representative for WOP as the wind lidar has no values very
285 close to the ground, while measurements extracted for 1100 m AGL are used as a proxy for the
286 vertical velocities at WFJ. The high resolution wind lidar data are grouped by hour and each
287 fitted to half-Gaussian probability density functions (PDFs) with zero mean and standard
288 deviation σ_w . An hourly PDF of updraft velocities is provided in the supplementary material as
289 an example of the calculation method we followed here (supplement Fig. S2). Employing the
290 “characteristic velocity” approach of Morales and Nenes (2010), the PDF-averaged values of
291 N_d and S_{max} are calculated by applying the parameterization using a single characteristic
292 velocity, $w^* = 0.79\sigma_w$. This approach has been shown to successfully predict cloud-scale values
293 of N_d in field studies for cumulus and stratocumulus clouds (e.g., Conant et al., 2004;
294 Meskhidze et al., 2005; Fountoukis et al., 2007; Kacarab et al., 2020). The droplet closure
295 carried out in this study is also used to support the validity of this approach for Alpine MPCs.
296 To determine the σ_w values used in the closure study (Section 3.2.1), we isolated the segments
297 of the wind lidar measurements that correspond to each cloud event observed by the
298 Holoballoon platform. The subsequent fitting of the measured updraft velocities to half-
299 Gaussian PDFs revealed a σ_w value representative of each cloud. The accuracy of the wind lidar
300 products is affected by precipitation, as the measured updraft velocities might be masked by
301 the terminal fall velocity of the hydrometeors. We therefore use disdrometer measurements to
302 identify and exclude precipitating periods from our analysis—~~using disdrometer measurements~~
303 ~~to constrain periods of precipitation~~. Aiming to examine how N_d responds to different vertical
304 velocity-aerosol situations, as a sensitivity test, potential N_d for both sites are calculated at 10
305 values of σ_w between 0.1 and 1.0 ms^{-1} that cover the observed range (Section 3.2.4). Note that
306 we use the term “potential” droplet number throughout this study, as its calculation is
307 performed regardless of the actual existence of clouds over the measurement sites.

308

309 3. Results and discussion

310 3.1 Particle number, CCN concentration and κ at WOP and WFJ

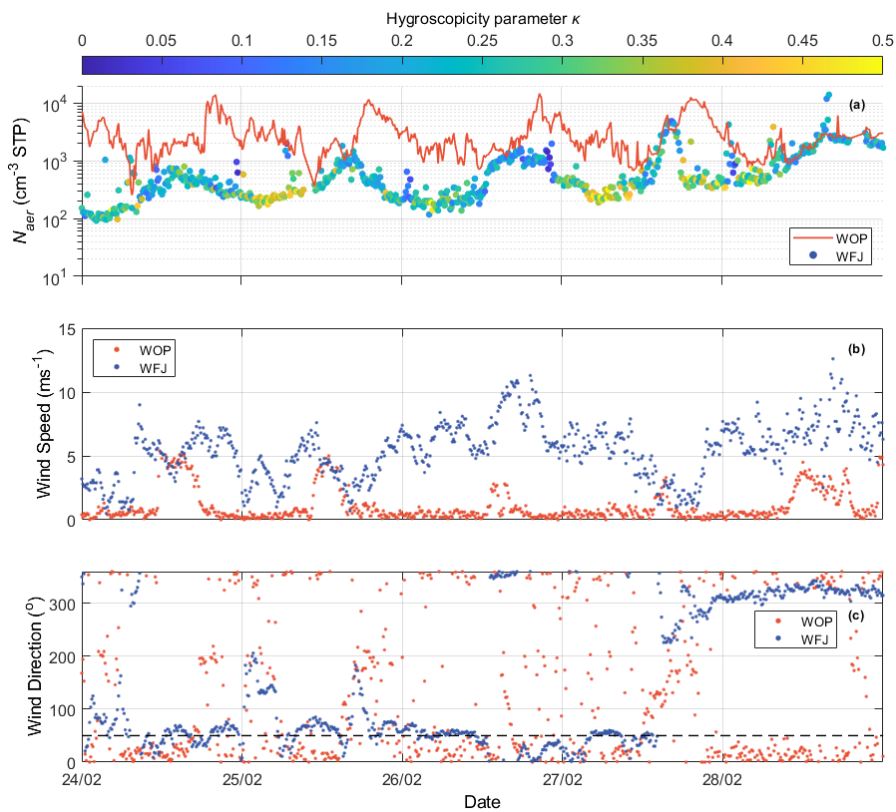
311 The total aerosol number concentration (N_{aer}) timeseries (integrated aerosol size distribution)
312 together with horizontal wind speed and direction measurements are depicted for both sites in
313 Figure 1. The N_{aer} data points of WFJ are colored by κ (Section 2.2), while the orange solid
314 line is used as a trace for WOP timeseries, as κ was not determined for the site owing to a lack

315 of corresponding CCN measurements. Aiming to interpret the aerosol variations and the
316 potential differences observed between valley and high-altitude measurements, the two-week
317 period of interest is divided into two different sub-periods. During 24 and 28 of February, a
318 high-pressure system was dominant over Europe with clear skies and elevated temperatures
319 (supplement Fig. S3). During this first sub-period, the N_{aer} varies considerably, and tends to
320 follow a diurnal cycle that anticorrelates between the two sites (Fig. 1a). The concentrations at
321 WOP are most of the times elevated with respect to WFJ, which is expected as the N_{aer} in the
322 valley is higher – being influenced by local sources, which during this time of the year include
323 emissions from biomass burning (BB) (Lanz et al., 2010). N_{aer} at WOP peaks in the evening,
324 reaching up to $\sim 10^4 \text{ cm}^{-3}$ presumably because of BB emissions in the valley which seem to
325 stop around midnight (Fig. 1a). Up to 2 orders of magnitude lower N_{aer} is measured at the same
326 time at the WFJ site. In the afternoon, aerosol concentrations at WFJ approach those observed
327 at WOP, indicating that the two sites are possibly experiencing similar air masses. The κ for
328 WFJ seems to follow a clear temporal pattern as well, ranging between ~ 0.1 - 0.4 with a
329 minimum in the afternoon, when the two sites experience the same air masses. Low N_{aer} values
330 are accompanied by higher κ , while at higher N_{aer} conditions less hygroscopic aerosols are
331 recorded (Fig. 1a).

332 The above diurnal cycles and their relationships can be understood in terms of BL
333 dynamics typically occurring in mountain-valley systems (Chow et al., 2013). During daytime,
334 under clear sky conditions, the slopes and the valley itself are warmed by solar radiation,
335 causing rising of the BL, and additionally the production of buoyant air masses that rise up the
336 slope toward the summit (through “up-slope” and “up-valley” winds) (Okamoto and Tanimoto,
337 2016). This hypothesis can be further supported by the fair weather recorded by the weather
338 station at WFJ until 28 February (supplement Fig. S3). The buoyant upslope flow could then
339 transport polluted air masses originating from the BL of the valley up to the WFJ site, elevating
340 the concentrations of less hygroscopic aerosols observed in the afternoon. The situation
341 reverses during nighttime, when cold air descends from the slopes (down-slope winds) and
342 flows out of the valley (down-valley winds) due to the radiative cooling of the surface. The
343 less polluted air observed during the early hours of the day before sunrise indicates that the
344 WFJ station remained in the free troposphere (FT), with lower N_{aer} and more aged air (i.e.,
345 larger κ) with a more prominent accumulation mode (Baltensperger et al., 1997; pp. 376-378
346 in Seinfeld and Pandis, 2006; Kammermann et al., 2010; Jurányi et al., 2011).

347 Another consideration is that the upslope flow that “connects” the valley and the
348 mountain-top site may not only be driven by thermal convection but also from mechanically-

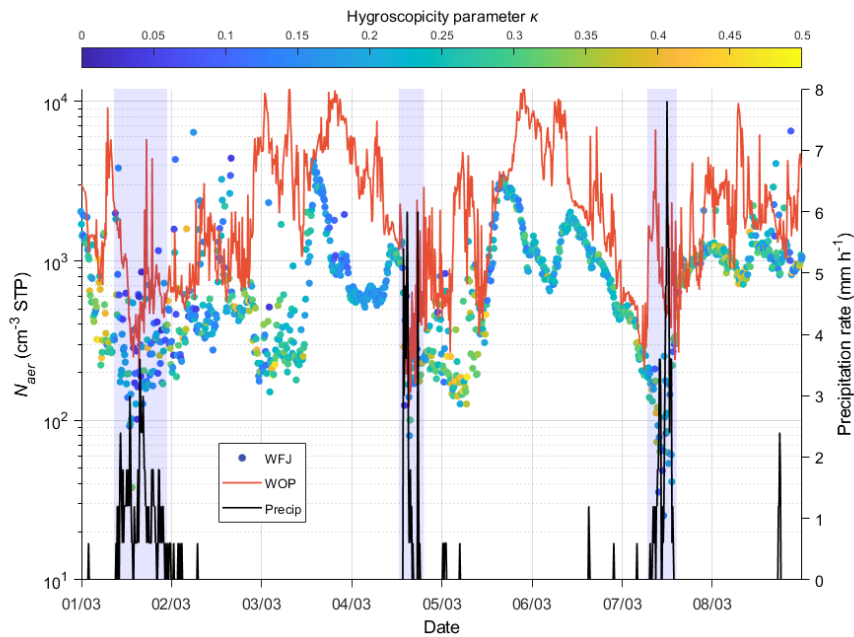
349 forced lifting. The latter mechanism is caused by the deflection of strong winds by a steep
 350 mountain slope and it can be of great importance depending mainly on the height of the
 351 mountain and the mean speed of the wind (Kleissl et al., 2007). The local wind effects can be
 352 further interpreted looking at the MeteoSwiss timeseries of wind speed and direction for both
 353 stations (Fig. 1b, c). Wind measurements at WFJ station recorded a strong wind speed reaching
 354 up to $\sim 11 \text{ ms}^{-1}$ from easterly-northeasterly directions between 24 and 28 of February. The wind
 355 direction measured at WFJ coincides with the relative location of WOP site (see black dashed
 356 line in Fig. 1c). The steep orography over the Alps would transform part of this strong
 357 horizontal motion into vertical motion, and transport air from WOP to WFJ, as seen in other
 358 Alpine locations, like Jungfrauoch (e.g., Hoyle et al., 2016). A detailed analysis however is
 359 out of the scope of this study.
 360



361
 362 **Figure 1.** (a) N_{aer} in standard temperature and pressure conditions (cm^{-3} STP) at WOP (orange
 363 line) and at WFJ (circles colored by κ), (b) wind speed (ms^{-1}), and (c) wind direction (in

364 degrees) obtained from the MeteoSwiss observation stations at WFJ (blue dots) and Davos
 365 (orange dots) between 24 and 28 February 2019. The black dashed line indicates the relative
 366 direction of WOP to WFJ. Each day is referenced to 00 UTC.

367
 368



369
 370 **Figure 2.** N_{aer} (cm^{-3} STP) at WOP (orange line) and at WFJ (circles colored by κ). The black
 371 solid line represents the precipitation rate (mm h^{-1}) recorded from the MeteoSwiss observation
 372 station for each 10-min interval at WFJ between 1 and 8 of March 2019. The blue-shaded areas
 373 represent the periods when precipitation recorded at WFJ site is most intense.

374
 375 Similar to Figure 1a, Figure 2 illustrates the N_{aer} timeseries measured at both sites along
 376 with the precipitation rate recorded by the MeteoSwiss station at WFJ during the time period
 377 between 1 and 8 March 2019. Meteorological observations show the pressure and temperature
 378 dropping (supplement Fig. S3) together with intense snow and rain events, associated with the
 379 passage of cold fronts over the region. Three intense precipitation events are visible in our
 380 dataset occurring on the 1st, 4th and 7th of March 2019 (blue-shaded areas on Fig. 2) creating
 381 up to 7.8 mm per hour of precipitation. The most intense drop in N_{aer} is seen to occur during
 382 and after the precipitation events, with the aerosol concentrations dropping to less than 200 cm^{-3}
 383 (100 cm^{-3}) at WOP (WFJ). This is not the case for the last event, where a big “spike” of N_{aer}
 384 is observed before the precipitation event in WOP timeseries, which is in contrast with the

385 concurrent sharp decrease in N_{aer} ($< 20 \text{ cm}^{-3}$) observed at WFJ. This could be an indication of
386 a local source affecting the N_{aer} recorded in the valley. During dry weather conditions, we can
387 notice again the aerosol timeseries correlating during the afternoon and anticorrelating later in
388 the evening-early morning hours. On March 3, a steep increase in N_{aer} is seen in WFJ timeseries
389 reaching up to $\sim 4000 \text{ cm}^{-3}$, which is followed by a period of several hours with low
390 hygroscopicity values ($\kappa < 0.2$) indicating once more the influence of freshly emitted particles
391 arriving at WFJ from the BL of lower altitudes. Additionally, between 1 and 8 March, the
392 diurnal cycle of particle hygroscopicity is less pronounced compared to the period between 24
393 and 28 February. Especially on the 1st and 7th of March, less hygroscopic aerosols ($\kappa < 0.1$) —
394 hence less effective CCN particles — are found at WFJ (Fig. 2). This is likely from either
395 precipitation removing aerosol through diffusive and impaction processes, or, the removal of
396 aerosol particles that first activate and then are removed by precipitation. Also, because N_{aer}
397 drops, fresh local emissions become more important, further justifying the predominance of
398 low hygroscopicity values.

399 Figure 3 presents the CCN number concentration timeseries measured at ambient
400 conditions at WFJ for all 6 supersaturations. Throughout the two-week measurement period
401 the recorded CCN number concentrations do not seem to follow a clear temporal pattern. The
402 absence of a diurnal cycle in CCN properties measured at Jungfraujoch during winter was also
403 pointed out in the study of Jurányi et al. (2011), because the site is mainly in free tropospheric
404 conditions during most of the winter. According to Figure 3, the observed CCN concentrations
405 tend to be low ($\sim 10^2 \text{ cm}^{-3}$) even at the highest SS (0.74%), which is expected given that WFJ
406 is a remote continental measurement site with CCN concentrations that are typical of free
407 tropospheric continental air (Jurányi et al., 2010, 2011; Hoyle et al., 2016; Fanourgakis et al.,
408 2019). This is again in line with the measured monthly median values of CCN (at SS = 0.71%)
409 reported by Jurányi et al. (2011) being equal to 79.1 and 143.4 cm^{-3} for February and March
410 2009, respectively. Some local CCN spikes are however recorded during the evening of 28
411 February and at the beginning of March (e.g., on 2nd, 4th and 6th March), with the observed
412 values of CCN reaching up to 650 cm^{-3} at SS=0.09% (lowest SS) and 1361 cm^{-3} at SS=0.74%
413 (highest SS). Considering that WFJ is a site frequently located in the FT, sudden fluctuations
414 in the CCN concentrations could be related to the vertical transport of freshly emitted particles
415 (e.g., wood burning or vehicle emissions) from the valley floor in Davos. It is also worthy to
416 note that some aerosol spikes observed on the 3rd ($\sim 3350 \text{ cm}^{-3}$) and the 5th of March (~ 2100
417 cm^{-3}) in the WFJ timeseries (Fig. 1a) are not accompanied by a corresponding peak in the CCN

418 timeseries. This indicates the presence of small aerosol particles, which activate above 0.74%
 419 supersaturation (i.e., particles with a diameter smaller than ~ 25 nm). This event could also be
 420 associated with new particle formation (NPF) events. A previous study by Herrmann et al.
 421 (2015) reported the aerosol number size distribution at the Jungfraujoch over a 6-year period
 422 indicating that NPF was observed during 14.5% of the time without a seasonal preference.
 423 Tröstl et al. (2016) also showed that NPF significantly adds to the total aerosol concentration
 424 at Jungfraujoch and is favored only under perturbed FT conditions (i.e., BL injections).
 425 Finally, during the three intense precipitation events (on 1st, 4th and 7th March) we can identify
 426 again that the wet removal of the more hygroscopic aerosol (Fig. 2) suppresses the presence of
 427 cloud-activating particles, at times depleting the atmosphere almost completely from CCN
 428 (Fig. 3). This is clearly shown on the 1st and the 7th of March, when the CCN number measured
 429 at 0.74% supersaturation drops below 10 cm^{-3} , which is extremely low for BL concentrations.

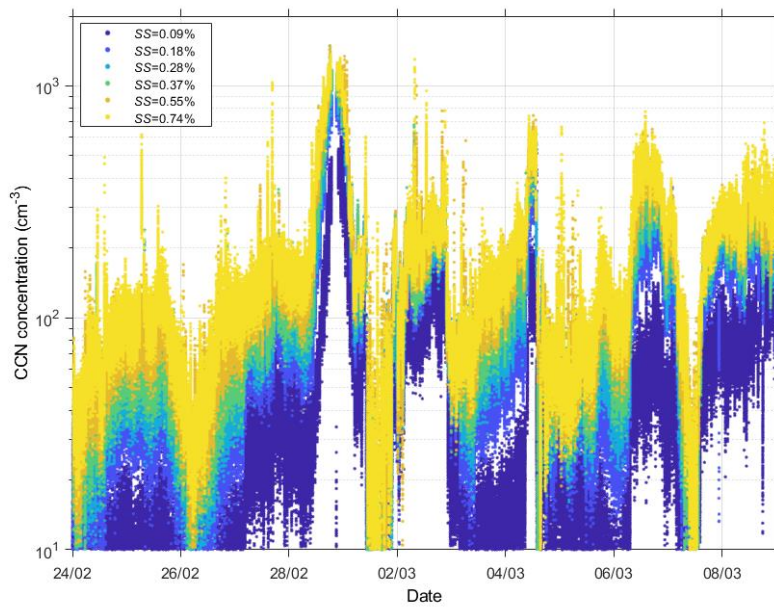
430 The aerosol hygroscopicity parameter derived from all CCN data collected between 24
 431 of February and 8 of March is presented in Figure 4a. The red solid line represents the hourly
 432 averaged hygroscopicity values over one complete instrument supersaturation cycle. The
 433 hygroscopic properties of the particles at WFJ vary as a function of supersaturation, exhibiting
 434 on average lower values (~ 0.1) at high SS and higher values (~ 0.3) at the lower SS . Since the
 435 supersaturation inversely depends on particle size, Figure 4a indicates that the hygroscopicity
 436 of the particles drops by almost 60% as the particles are getting smaller (i.e., as the
 437 supersaturation increases). Table 2 summarizes the mean values of κ and D_{cr} and their standard
 438 deviations, as calculated for each measured SS . The anticorrelation seen between the instrument
 439 SS and D_{cr} is reasonable, if we consider that the latter represents the minimum activation
 440 diameter in a population of particles, and therefore only the particles with a $D_{cr} > 193.54$ nm
 441 are able to activate into cloud droplets at low SS values (0.09%). The hourly averaged
 442 hygroscopicity κ at each SS slot falls within a range of ~ 0.2 and ~ 0.3 , which is a well
 443 representative value of continental aerosols (Andreae and Rosenfeld, 2008; Rose et al., 2008).

444 **Table 2.** Average κ and D_{cr} values at WFJ for each SS measured between 24 February and 8
 445 March 2019. Uncertainty for each value is expressed by the standard deviation.

SS (%)	κ_{mean}	$D_{cr,mean}$
0.09	0.26 ± 0.10	193.54 ± 29.58
0.18	0.31 ± 0.13	116.80 ± 22.20
0.28	0.25 ± 0.13	96.69 ± 21.62

0.37	0.24 ± 0.13	82.67 ± 20.93
0.55	0.20 ± 0.12	68.30 ± 20.95
0.74	0.19 ± 0.11	58.11 ± 17.54

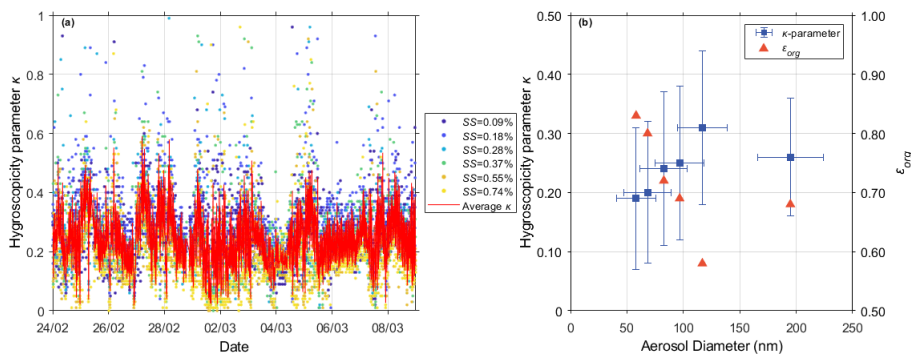
446



447

448 **Figure 3.** Timeseries of in-situ CCN number concentrations (cm^{-3}) at WFJ for different levels
 449 of supersaturation (SS) with respect to water between 24 February and 8 March 2019.

450



451
 452 **Figure 4.** (a) Timeseries of the hygroscopicity parameter κ at WFJ at different levels of
 453 instrument supersaturation SS (0.09–0.74%) throughout the period of interest. The red solid red
 454 line indicates the hourly averaged κ timeseries over a complete SS cycle. (b) Size-resolved
 455 aerosol hygroscopicity (blue squares) and the respective ϵ_{org} (orange triangles) calculated for
 456 the WFJ site.

457
 458 The hygroscopicity parameter κ along with the inferred ϵ_{org} (Eq. 2) ~~is~~ are shown in Figure
 459 4b as a function of particle size. Compared to smaller particles, the higher κ of larger particles
 460 (>100 nm) is consistent with them being more aged and with a lower fraction of organics. The
 461 smaller particles are possibly enriched in organic species, which is consistent with the notion
 462 that air masses in the valley can contain large amounts of freshly emitted BB smoke with lower
 463 κ . Aerosol particles in the FT are considerably more aged (pp. 376–378 in Seinfeld and Pandis,
 464 2006) and exhibit higher values of κ and consequently lower values of ϵ_{org} . The chemical
 465 composition of sub-100 nm particulate matter was therefore presumably dominated by organic
 466 material transported from the valley, while the higher κ values characterizing the larger
 467 particles are consistent with the more aged character of free tropospheric aerosols (e.g., Jurányi
 468 et al., 2011). The higher ϵ_{org} inferred for the smaller particles suggests that mixing between
 469 fresh emissions in the valley and the free tropospheric aerosol might also be taking place at
 470 WFJ.

471
 472 **3.2 Potential cloud droplet number concentration and maximum supersaturation**

473 **3.2 Droplet formation in the Alpine region**
 474 **3.2.1 Method evaluation against direct observations**

475 During the RACLETS campaign, planar and dendritic ice particles were collected from
 476 supercooled clouds at WFJ aiming to examine their refreezing ability. A detailed description

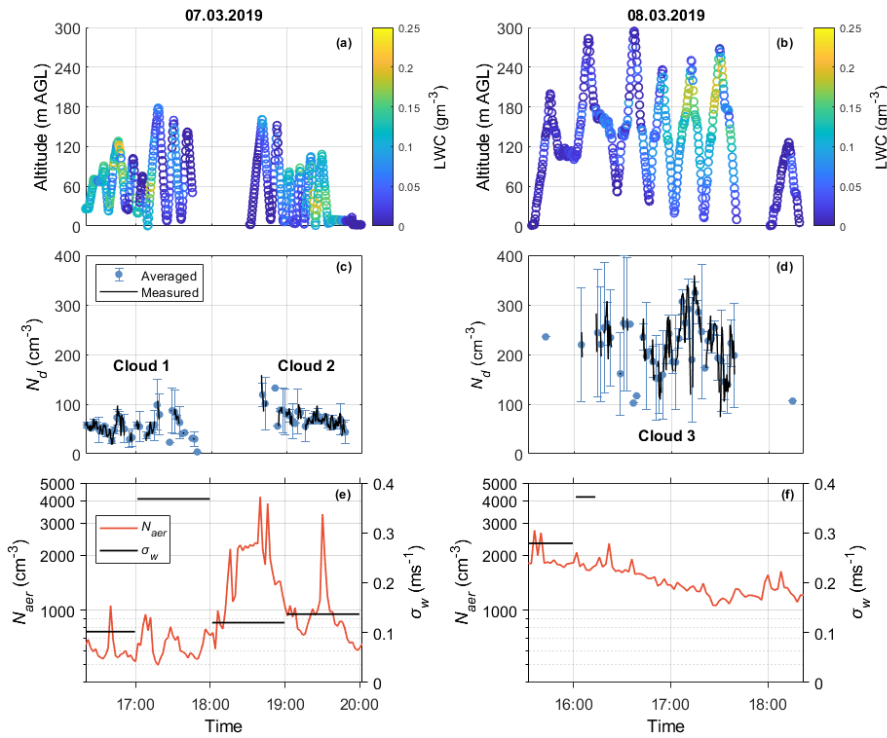
Formatted: Font: Italic

477 of the sampling methodology can be found in Mignani et al. (2019). Between ~~March-1~~ and
478 ~~March-7~~ March, images of single dendrites were taken and analyzed visually for the degree of
479 riming (supplement Fig. S4). The estimated riming degree varies from 1 (lightly-rimed) to 4
480 (heavily-rimed) following the categorization of Mosimann et al. (1994). Some representative
481 images of each measured riming degree are shown in Figure S4b. Although images were
482 captured intermittently, they were taken within all three intense precipitating events occurring
483 during the period of interest (blue-shaded areas on Fig. 2). All dendrites captured were at least
484 lightly rimed (i.e., riming degree = 1), which provides direct evidence for the co-existence of
485 supercooled droplets and ice in clouds. Except the indirect evidence of the presence of MPCs
486 over WFJ, Figure 5 provides an overview of the direct microphysical measurements carried
487 out by the Holoballoon at WOP (Section 2.1.3). Three cloud events are sampled during the 7th
488 and the 8th of March, a more detailed description of which can be found in Ramelli et al. (~~2020b~~,
489 e2021a, b). The observed low-level clouds are likely produced by orographic lifting when the
490 low-level flow is forced to ascent over the local topography from Klosters to WOP producing
491 local updrafts and thus water supersaturated conditions. The cloud LWC measurements from
492 the holographic imager display significant temporal variability that is also related to variations
493 in the altitude of the tethered balloon system, as it tends to follow an adiabatic profile (Fig. 5a,
494 b). Deviations from the adiabatic LWC profile are likely caused by entrainment of dry air
495 within the low-level clouds. Departures during the mixed-phase conditions recorded on March
496 8 (Fig. 5b), could also be attributed to the depletion of N_d through riming and depositional
497 growth. These two processes are frequently found to enhance orographic precipitation in feeder
498 clouds. Indeed, a large fraction of rimed ice particles and graupel were observed that day with
499 HOLIMO between 17:00 and 17:40 UTC (Ramelli et al., ~~2020e2021b~~). Throughout the two-
500 day dataset presented in Figure 5, the HoloBalloon system samples at altitudes lower than 300
501 m AGL, providing observations that are representative of BL conditions.

502 The observed N_d timeseries collected at WOP are illustrated in Figures 5c and 5d. The
503 measurements corresponding to $LWC < 0.05 \text{ gm}^{-3}$ are filtered out from the analysis, assuming
504 that they do not effectively capture in-cloud conditions. A similar criterion for LWC was also
505 applied in Lloyd et al. (2015) to determine the periods when clouds were present over the
506 Alpine station of Jungfraujoch. Since the measured cloud properties have finer resolution (10-
507 20 secs) than the predicted ones, the observed dataset is averaged every 2 minutes. On March
508 7, the balloon-borne measurements were taken in a post-frontal air mass (i.e., passage of a cold
509 front in the morning) and indicated the formation of two low-level liquid layers (Fig. 5c) over
510 WOP, which is attributed to low-level flow blocking (Ramelli et al., ~~2020b2021a~~). Note that

511 small droplets ($< 6 \mu\text{m}$) cannot be detected by HOLIMO (Section 2.3.1) and therefore the
 512 reported N_d should be considered as a lower estimate. The influence of small cloud droplets,
 513 however, on the reported LWC is minor, since the contribution of the larger cloud droplets
 514 dominates. During the first cloud event, an N_d of up to $\sim 100 \text{ cm}^{-3}$ was recorded, while slightly
 515 increased N_d in the range of $\sim 50\text{-}120 \text{ cm}^{-3}$ is visible during the second cloud event. On March
 516 8, a small-scale disturbance passed the measurement location Davos, which brought
 517 precipitation (Ramelli et al., 2020e2021b). During the passage of the cloud system, the in-situ
 518 measurements collected at WOP revealed the presence of a persistent low-level feeder cloud
 519 confined to the lowest 300 m of the cloud. The mixed-phase low-level cloud that is shown in
 520 Figure 5d, turned into an ice-dominated low-level cloud after 18 UTC (not shown). Throughout
 521 this event, N_d seems to range between $\sim 100\text{-}350 \text{ cm}^{-3}$ (Fig. 5d), while the observed ICNC was
 522 in the range of $\sim 1\text{-}4 \text{ L}^{-1}$ (see Fig. 6b in Ramelli et al., 2020e2021b).

523



524

525 **Figure 5.** Timeseries of the 7th (left panels) and the 8th (right panels) of March, showing the
 526 vertical profiles of the LWC (gm^{-3}) in (a) and (b), the filtered (black lines) and the 2-minute
 527 averaged (cyan circles) N_d (cm^{-3}) measured at WOP with the HoloBalloon platform in (c) and
 528 (d), and the corresponding SMPS aerosol concentrations (cm^{-3}) (orange line) and the hourly

529 wind-lidar derived σ_w values (ms^{-1}) (black line) in (e) and (f). Error bars represent the standard
530 deviation of N_d during the averaging period.

531

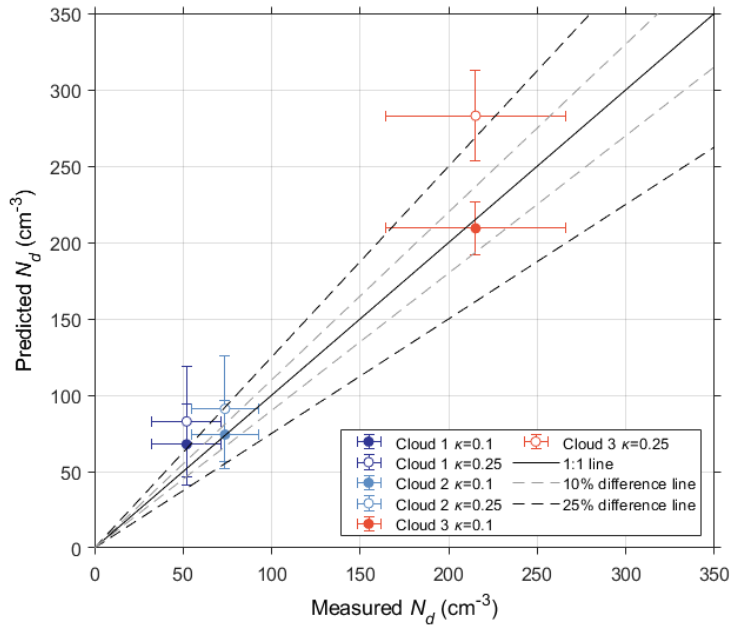
532 According to Figures 5e and 5f, low N_{aer} ($<10^3 \text{ cm}^{-3}$) and intermediate highly variable
533 σ_w values (~ 4 times higher σ_w after 17:00) are representative of the period throughout which
534 the first cloud formed, while up to 4 times higher N_{aer} is observed during the following two
535 cloud events, with relatively low σ_w values characterizing the second cloud compared to the
536 third one. On March 8, the disdrometer recorded rainfall over WOP, starting a few minutes
537 after the development of the observed cloud system, reflected in the removal of updraft velocity
538 measurements after 16:15 (Fig. 5f). Note that the concentration measurements presented in
539 Figure 5 correspond to ambient temperature and pressure conditions. The contrasted aerosol
540 and vertical velocity regimes, in which the observed clouds are formed, offer a great
541 opportunity to test how the proposed methodology performs under a wide range of aerosol and
542 velocity conditions. Indeed, the mean cloud droplet diameters exhibit a wide range of values,
543 which for WOP range between $10 \mu\text{m}$ and $17 \mu\text{m}$ on March 7, and $8 \mu\text{m}$ to $12 \mu\text{m}$ on March 8
544 (not shown).

545 The N_d closure performed for the three cloud events observed over WOP during the last
546 two days of the period of interest is presented in Figure 6. Note that the potential droplet
547 formation predicted N_d is evaluated using the updraft velocity PDF calculated for each cloud
548 period, rather than the hourly σ_w data shown in Figures 5e and 5f (Section 2.3). Owing to the
549 precipitation occurrence during March 8, we focused on the 15-min time period between 16:00
550 and 16:15 to determine a relevant updraft velocity from the wind lidar measurements
551 representative of Cloud 3. The Gaussian fit to the updraft velocities gave a distribution with σ_w
552 = 0.24 and 0.16 ms^{-1} for the first two clouds present on the 7th of March, and, $\sigma_w = 0.37 \text{ ms}^{-1}$
553 for the cloud system observed on the 8th of March. The w^* values used to apply the droplet
554 parameterization are therefore between 0.1 - 0.4 ms^{-1} (Section 2.3). Figure 6 indicates that the
555 parameterization predictions agree to within 25% with the in-situ cloud droplet number
556 concentrations. A similar degree of closure is frequently obtained for other in-situ studies (e.g.,
557 Meskhidze et al., 2005; Fountoukis et al., 2007; Morales et al., 2011; Kacarab et al., 2020),
558 which however focused on liquid-phase clouds. Here we show that the methodology can also
559 work for MPCs (i.e., Cloud 3 in Fig. 6). It is important to note here that part of the discrepancy
560 between prediction and measurement could also be related to the underestimation of the
561 measured N_d (Section 2.1.3). Hence, an even better degree of closure is likely. Also, the derived
562 σ_w value used to calculate the predicted N_d for Cloud 1, might be biased low by the lower σ_w

563 values recorded before 17:00 (Fig. 5e). Nevertheless, the updraft averaging used in the droplet
564 closure study corresponds to the measured N_d averaging time period, and therefore, we do not
565 expect the degree of closure to be affected.

566 The good agreement between measurements and predictions -- even under mixed-phase
567 conditions, reveals that processes like condensation freezing and the removal of cloud droplets
568 through riming and collision-coalescence for the clouds considered are not disturbing the S_{max}
569 and hence the N_d predicted by the parameterization, at least for the given clouds. ~~Pre~~That said,
570 it is known that pre-existing liquid and ice hydrometeors falling to the examined cloud levels
571 might alsoactivation region of clouds can deplete the supersaturation affecting the number of
572 the activated droplets. ~~The contribution of -- and such~~ supersaturation depletion effects can
573 readily be included in the droplet activation parameterization (Sud et al., 2013; Barahona et al.,
574 2014) ~~but is not considered in this study if needed~~. Furthermore, the parameterization
575 predictions indicate that the best fit is achieved using a κ of ~ 0.1 (Fig. 6). N_{aer} at WOP is likely
576 dominated by lower κ values, indicating that the particles are getting richer in organic material,
577 compared to WFJ, which supports the aerosol analysis carried out in Section 3.1. These results
578 are robust, indicating that for non-precipitating BL clouds the proposed calculation method
579 captures cloud droplet formation at WOP and WFJ.

Formatted: Indent: First line: 0"



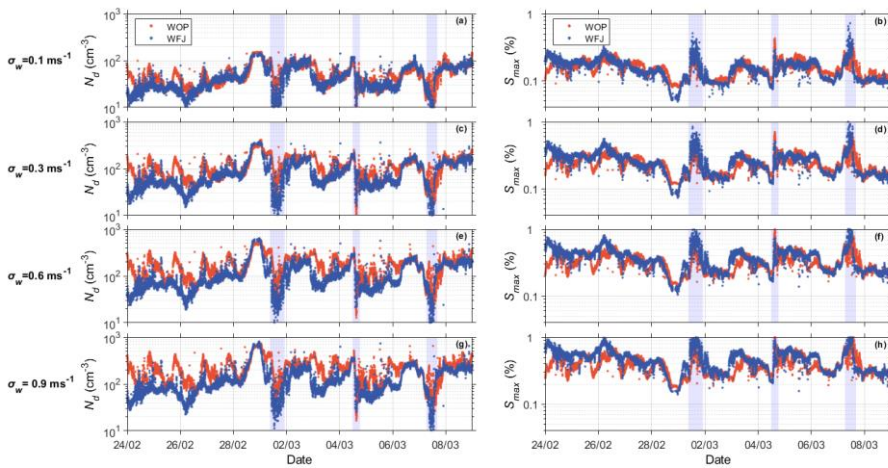
581
 582 **Figure 6.** Comparison between average predicted N_d (cm^{-3}) with the droplet activation
 583 parameterization and N_d (cm^{-3}) observed during the three cloud events on the 7th (blue and cyan
 584 circles) and the 8th of March (orange circles) 2019. For all three cloud events droplet closure is
 585 performed assuming a κ parameter of 0.1 (filled circles) and 0.25 (empty circles). The error
 586 bars represent the standard deviation of N_d during each cloud event.

587
 588 **3.2.2 Droplet/Potential droplet formation at WOP and WFJ**
 589 According to the methodology proposed in Section 2.3, using the in-situ measured N_{aer} , the
 590 estimated chemical composition and the observed updraft velocity range, we determine the
 591 potential N_d and S_{max} that would form over both measurement sites. At WOP, clouds are formed
 592 locally due to the local topography (Ramelli et al., ~~2020b~~, ~~e2021a, b~~), supporting the use of
 593 surface measured aerosol to estimate the potential N_d over this site. This is further supported
 594 by the good degree of droplet closure (Section 3.2.1). A similar closure study could not be
 595 repeated for WFJ owing to a lack of in-situ data, however the airmasses sampled (i.e., those
 596 given as input to the parameterization) are often in the FT, so they should contain the same
 597 aerosol as the one used to form the clouds. This does not apply under perturbed FT conditions,
 598 which are however accompanied by the presence of less hygroscopic particles over the
 599 mountain-top site and are less likely related to cloud formation (Section 3.1). Here we assume
 600 a κ of 0.25 to calculate the potential droplets for WFJ according to our CCN-derived

601 hygroscopicity values (Table 2) and given that S_{max} usually ranges between ~ 0.1 - 0.3% . In
602 estimating the potential droplets for WOP, we use a κ of 0.1 given that aerosol is likely strongly
603 enriched in organics; the good degree of closure that this value supports its selection (Section
604 3.2.1). Figure 7 depicts the potential N_d and the corresponding S_{max} timeseries calculated at
605 ambient conditions for WOP (orange dots) and WFJ (blue dots) using cloud updraft velocities
606 that are indicative of the observed σ_w range (Section 3.4), namely 0.1, 0.3, 0.6 and 0.9 ms^{-1} .
607 The same behavior is seen for all four σ_w values selected while, as expected, larger values of
608 N_d and S_{max} are achieved at higher σ_w . During the first days of the period of interest, the
609 calculated N_d at WOP (Fig. 7a, c, e, g) is up to 10 times larger than at WFJ, despite the lower
610 κ values characterizing its aerosol population. WFJ tends to have lower N_d due to the lower
611 N_{aer} recorded. It is also important to highlight the anticorrelation between S_{max} and N_d values
612 arising from the nonlinear response of droplet number and maximum cloud parcel
613 supersaturation to fluctuations in the available aerosol/CCN concentrations (Reutter et al.,
614 2009; Bougiatioti et al., 2016; Kalkavouras et al., 2019). Higher N_{aer} elevates N_d values. The
615 available condensable water is then shared among more growing droplets, depleting the
616 supersaturation. Even more interesting is the fact that until February 28 the calculated N_d
617 timeseries at WOP show a pronounced diurnal cycle, similar to the total N_{aer} timeseries (Section
618 3.1). Lower N_d values are visible during nighttime after midnight, presumably due to a paucity
619 of BB activities in the limited turbulence valley. Droplet concentrations at WFJ do not follow
620 a diurnal pattern in contrast to the aerosol data (Fig. 1a). However, the activation fraction (i.e.,
621 N_d/N_{aer}) at WFJ displays a clear diurnal variability until the end of February (supplement Fig.
622 S5).

623 Through comparison with the MeteoSwiss precipitation measurements at WFJ (Fig. 4),
624 it should be emphasized again that during the second sub-period of interest the occurrence of
625 precipitation is followed by a depression in N_d (Fig. 7a, c, e, g) and a concurrent increase in
626 S_{max} reaching up to $\sim 1\%$ (Fig. 7b, d, f, h). Especially at WFJ, N_d drops almost to zero on the
627 1st, the 4th and the 7th of March, when precipitation is most intense (blue-shaded areas in Fig.
628 2 and 7). These trends are related to the washout of hygroscopic material observed at WFJ (Fig.
629 2) leading to the extremely low CCN concentrations ($\sim 10 \text{ cm}^{-3}$) measured during these three
630 days. During the first two intense precipitation events, the N_{aer} is relatively high, compared to
631 the third event, with concentrations reaching up to $\sim 300 \text{ cm}^{-3}$ at both stations. The small
632 activation fraction (supplement Fig. S5) combined with the high S_{max} values indicates once
633 more that small particles that activate into cloud droplets only above 0.3 to 0.5% of

634 supersaturation are present at both stations. However, this behavior is not seen on March 7 at
 635 WFJ.
 636

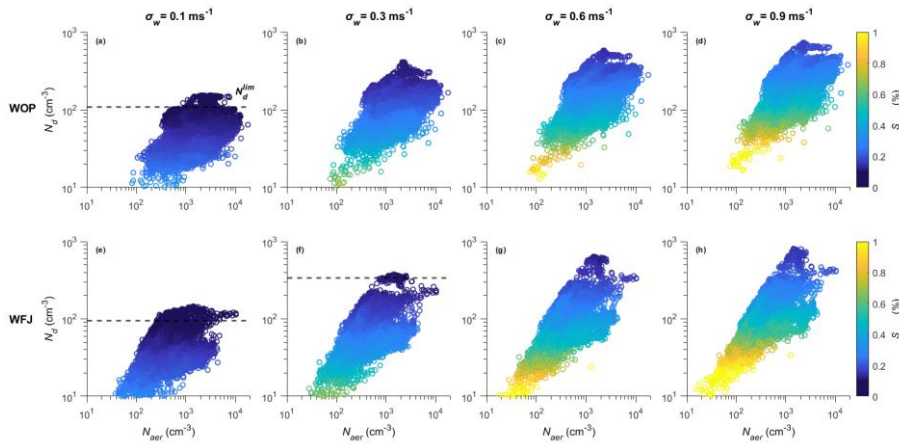


637
 638 **Figure 7.** Calculated timeseries of N_d (cm^{-3}) (left panels) and S_{max} (%) (right panels), for updraft
 639 velocities of $\sigma_w = 0.1 \text{ ms}^{-1}$ in a and b, 0.3 ms^{-1} in c and d, 0.6 ms^{-1} in e and f, and 0.9 ms^{-1} in g
 640 and h, during the period of interest at WOP (orange dots) and WFJ (blue dots). The blue-shaded
 641 areas represent the intense precipitating periods as shown in Figure 2.

642
 643 **3.2.3 Droplet behavior under velocity-limited conditions**

644 Combining the potential N_d and the corresponding S_{max} with the N_{aer} data yields important
 645 information on whether clouds are sensitive to vertical velocity or aerosol changes. Cloud
 646 studies (e.g., Jensen and Charlson, 1984; Twomey, 1993; Ghan et al., 1998, Nenes et al., 2001
 647 and Reutter et al., 2009) have long recognized the role of water vapor competition on droplet
 648 formation, while the success of mechanistic parameterizations for climate models relies on the
 649 ability to capture this effect accurately (e.g., Ghan et al., 2011; Morales and Nenes, 2014).
 650 Twomey (1993) discusses this conceptually and states that competition may be fierce enough
 651 to reduce N_d with increasing N_{aer} , which was later demonstrated by Ghan et al. (1998) to occur
 652 for mixtures of sulfate aerosol and sea spray. Reutter et al. (2009) did not focus on such extreme
 653 conditions of water vapor competition, but rather situations that are consistent with dominance
 654 of anthropogenic pollution in clouds. Indeed, for high N_{aer} , droplets in clouds become
 655 insensitive to aerosol perturbations, giving rise to the so-called “velocity limited cloud
 656 formation”. Figure 8 displays this, presenting the response of the calculated N_d to changes in

657 N_{aer} for a representative range of updraft velocities prevailing over WOP (top panels) and WFJ
 658 (bottom panels). The data are colored by the respective S_{max} achieved in cloudy updrafts. For
 659 low σ_w values (Fig. 8a, d) we can identify that above an N_{aer} of $\sim 300 \text{ cm}^{-3}$, the N_d at both
 660 stations reaches a plateau, where it becomes insensitive to further aerosol changes. At WFJ,
 661 the same behavior is seen for intermediate σ_w values and $N_{aer} \gtrsim 1000 \text{ cm}^{-3}$ (Fig. 8f). Kacarab et
 662 al. (2020) and Bougiatioti et al. (2020) examined a wide range of ambient size distributions
 663 and proposed that clouds became velocity-limited when S_{max} dropped below 0.1%. This reflects
 664 the increasingly fierce competition for water vapor during droplet formation, which allows only
 665 a few particles to activate into cloud droplets.



667
 668 **Figure 8.** In-situ N_d (cm^{-3}) vs. N_{aer} (cm^{-3}), for updraft velocities of $\sigma_w = 0.1 \text{ ms}^{-1}$ in a and e, 0.3
 669 ms^{-1} in b and f, 0.6 ms^{-1} in c and g and 0.9 ms^{-1} in d and h, during the period of interest at WOP
 670 (top panels) and WFJ (bottom panels). Data are colored by S_{max} (%).

671
 672 Building upon these findings, we used the ~~predicted~~calculated S_{max} as an indicator for
 673 aerosol- or velocity-limited conditions prevailing over the Alps. The horizontal dashed lines
 674 plotted on Figure 8 (a), (e) and (f) illustrate a plateau, where $S_{max} < 0.1\%$ and the modulation
 675 of the N_d is driven mostly by the cloud dynamics, hence the updraft velocity variability, rather
 676 than aerosol variations. This plateau is termed limiting droplet number (N_d^{lim}), following
 677 Kacarab et al. (2020), and is essentially the maximum N_d that can be formed under these vertical
 678 velocity conditions. The vertical-velocity regime is therefore strictly defined, whenever S_{max}
 679 drops below 0.1% and N_d approaches N_d^{lim} . Conversely, when S_{max} in clouds exceeds 0.1%,

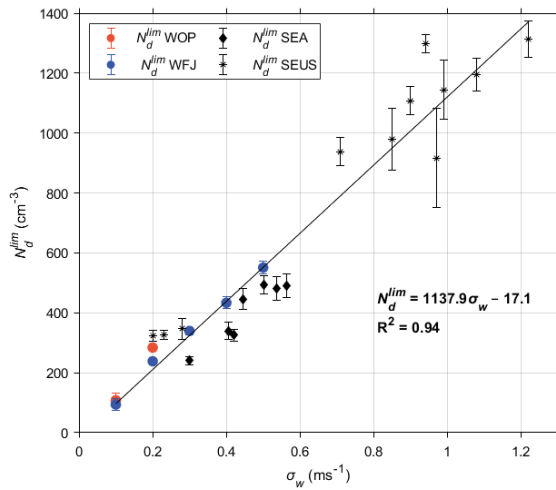
680 droplet formation in the BL of both measurement sites is in the aerosol-limited regime, as the
681 S_{max} is high enough for clouds to be responsive to aerosol changes.

682 An alternative way of examining the N_d^{lim} response to changes in σ_w is shown in Figure
683 9. It should be noted that the N_d^{lim} values shown on this figure are determined by calculating
684 the averaged N_d achieved whenever $S_{max} < 0.1\%$ for each examined σ_w value. At WOP, droplet
685 formation is in the velocity-limited regime only for low σ_w values, namely 0.1 and 0.2 ms^{-1} ,
686 when the activated particles have more time to deplete the gas phase, and the S_{max} reached is
687 that required to activate only the largest particles. At WFJ the prevailing dynamics create
688 velocity-limited conditions even for more turbulent boundary layers when σ_w reaches up to 0.5
689 ms^{-1} . N_d^{lim} (cm^{-3}) is linearly correlated with σ_w (ms^{-1}) which can be described as $N_d^{lim} =$
690 $1137.9 \sigma_w - 17.1$ (Fig. 9). As a result, doubling σ_w from 0.1 to 0.2 ms^{-1} increases N_d^{lim} by
691 $\sim 60\%$ for both sites, while transitioning from 0.2 to 0.4 ms^{-1} further increases N_d^{lim} by $\sim 45\%$,
692 and finally an additional $\sim 20\%$ increase in N_d^{lim} occurs for WFJ for the 0.4-0.5 ms^{-1} velocity
693 range. Remarkable agreement is seen for corresponding trends between N_d^{lim} and σ_w calculated
694 for marine Stratocumulus clouds formed under extensive BB aerosol plumes over the Southeast
695 Atlantic (SEA) Ocean (Kacarab et al., 2020), along with BL clouds formed in the Southeast
696 United States (SEUS) (Bougiatioti et al., 2020). Both studies have followed the same
697 probabilistic approach for computing N_d as the one followed here. This realization is important
698 as it implies that for regions where velocity-limited conditions are expected (i.e., under
699 particularly high particle loads), $N_d \sim N_d^{lim}$ and the $N_d^{lim} - \sigma_w$ relationship can be used to
700 diagnose σ_w from retrievals of droplet number for virtually any type of BL cloud, using a
701 number of established methods (e.g. Snider et al., 2017; Grosvenor et al., 2018).

702 3.2.4 σ_w and observed N_d determine if droplet formation is aerosol- or velocity-limited

703 Observations of N_d when compared against N_d^{lim} can potentially be used to deduce if droplet
704 formation is velocity- or aerosol-limited. This is important because it indicates whether aerosol
705 fluctuations are expected to result in substantial N_d responses in clouds. The strong correlation
706 between σ_w and N_d^{lim} enables this comparison. From the σ_w timeseries together with the linear
707 $N_d^{lim} - \sigma_w$ relationship (Section 3.2.3; Fig. 9) we obtain estimates of N_d^{lim} for both
708 measurement stations (black dashed line in Fig. 10a, b) and the ratio N_d/N_d^{lim} (magenta dotted
709 lines in Fig. 10a, b). The N_d timeseries calculated for WOP tend to be approximately one third
710 of N_d^{lim} for most of the observational period (colored circles in Fig. 10a, b), while for WFJ the
711

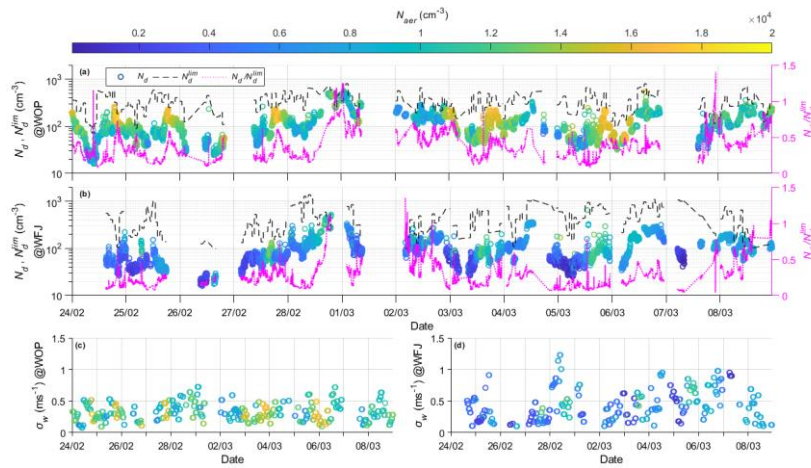
712 same ratio is even lower $\sim 1/4$. Focusing on the relatively short periods when S_{max} values drop
 713 below 0.1%, we estimate that droplet formation over both measurement sites enters a velocity-
 714 limited regime when the ratio N_d/N_d^{lim} exceeds a critical value of 0.65, with the most prevalent
 715 value being at ~ 0.9 (supplement Fig. S6).



716

717 **Figure 9.** Limiting droplet number N_d^{lim} (cm^{-3}) against the standard deviation of updraft
 718 velocities σ_w (ms^{-1}), calculated when vertical-velocity-limited conditions are met over at WOP
 719 (orange circles) and WFJ (blue circles) sites throughout the period of interest. Superimposed
 720 are the corresponding values calculated for clouds forming over the SEA Ocean (rhombuses)
 721 and over the SEUS (asterisks).

Formatted: Font color: Auto



722 **Figure 10.** Timeseries of potential N_d (cm^{-3}) (circles colored by N_{aer}) along with N_d^{lim} (cm^{-3})
 723 (black dashed line) and the ratio between those two (i.e. N_d/N_d^{lim}) (magenta dotted line),
 724 together with the timeseries of the calculated standard deviation of updraft velocities (ms^{-1})
 725 (circles colored by N_{aer}), as estimated for WOP (a, c) and WFJ (b, d).

727 Throughout the period of interest velocity-limited conditions are met at WOP (WFJ)
 728 with a frequency of $\sim 0.5\%$ ($\sim 2.5\%$) of the total time, reflecting again the sensitivity of droplet
 729 formation to aerosol fluctuations. During nighttime however, when lower σ_w values ($\sim 0.1 \text{ ms}^{-1}$)
 730 are recorded at WOP (Fig. 10c), we can observe some short periods characterized by
 731 intermediate to high N_{aer} ($> 1000 \text{ cm}^{-3}$) when the ratio N_d/N_d^{lim} exceeds ~ 0.65 , indicating that
 732 droplet variability is driven by updraft velocity. The σ_w values calculated at WFJ do not display
 733 a clear temporal pattern (Fig. 10d) but are generally higher than those recorded at the valley
 734 site. This is expected considering the steepness of the topography than can cause updraft
 735 velocities to be higher, especially for air-masses approaching the site from the north-easterly
 736 directions. Over the high mountain-top site cloud formation is in the velocity-limited regime
 737 (i.e. $N_d/N_d^{lim} > 0.65$) under high N_{aer} ($\sim 1500 \text{ cm}^{-3}$) and higher σ_w conditions (~ 0.8
 738 ms^{-1}). These conditions can be created when polluted air-masses from the valley site are
 739 vertically transported to WFJ.

Formatted: Left, Line spacing: single

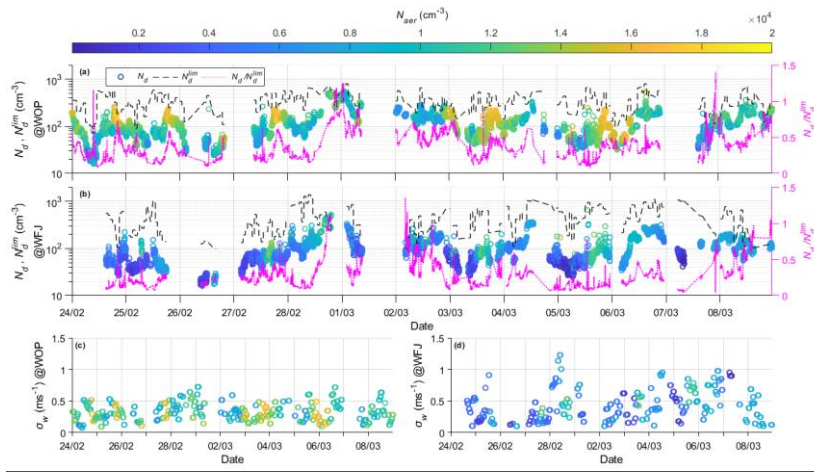


Figure 10. Timeseries of potential N_d (cm^{-3}) (circles colored by N_{aer}) along with N_d^{lim} (cm^{-3}) (black dashed line) and the ratio between those two (i.e., N_d/N_d^{lim}) (magenta dotted line), together with the timeseries of the calculated σ_w (ms^{-1}) (circles colored by N_{aer}), as estimated for WOP (a, c) and WFJ (b, d).

4. Summary and conclusions

The current study focuses on the aerosol-CCN-cloud droplet interplay in Alpine clouds sampled during the RACLETS field campaign over a two-week period of measurements conducted in the valley (WOP), and at the mountain-top station (WFJ). Our main objective was to investigate the drivers of droplet formation in MPCs formed in the region and understand in which situations N_d is sensitive to aerosol perturbations.

Overall, lower N_{aer} was systematically recorded at WFJ, indicating that the site is influenced by FT conditions. Deviations from this behavior are observed during fair weather conditions, when injections from the BL of lower altitudes can cause up to an order of magnitude elevation in the N_{aer} measured at WFJ. Combining the particle size distribution and CCN number concentration measured at WFJ, the average hygroscopicity parameter κ is about 0.25, consistent with expectations for continental aerosol. The size-dependent κ reveals that accumulation mode particles are more hygroscopic than the smaller ones, which we attribute to an enrichment in organic material associated with primary emissions in the valley. The hygroscopicity of the particles at WFJ exhibit variations until February 28, which could reflect BL injections from the valley. Precipitation events occurring between 1 and 8 March, efficiently decrease N_{aer} , sometimes leaving some less hygroscopic particles.

765 Wind lidar products collected at WOP constrain the PDF of updraft velocities, which
766 combined with observed size distributions and hygroscopicity can be used to calculate the N_d
767 in clouds. We show predictions to agree within 25% with the limited observations of N_d
768 available. While this degree of closure has been achieved in past studies for liquid-phase
769 clouds, it has not been done at temperatures below freezing and with clouds containing ice –
770 as done here.

771 Combining the potential N_d and the corresponding S_{max} with the aerosol size distribution
772 data we sought to identify regimes where clouds formed are aerosol- or velocity-limited. We
773 found that when sufficient aerosol is present to decrease S_{max} below 0.1%, Alpine clouds
774 become velocity-limited, with the N_d reaching an upper limit, $N_d^{lim} \sim 150-550 \text{ cm}^{-3}$, that
775 depends on σ_w . Velocity-limited conditions occur when N_d/N_d^{lim} is above 0.65. Based on this
776 understanding, we deduce that droplet formation throughout the period of interest appears most
777 of the time to be aerosol-limited. More specifically, at the valley site, WOP, clouds become
778 sensitive to updraft velocity variations only during nighttime, when the BL turbulence is low.
779 Conversely, velocity-limited conditions are encountered at WFJ, during periods characterized
780 by elevated aerosol and CCN concentration levels ($>10^3 \text{ cm}^{-3}$) and higher σ_w values ($\sim 0.8 \text{ ms}^{-1}$).
781 Although variations in vertical velocity have not always been found to be the strongest factor
782 influencing the cloud microphysical characteristics, correct consideration of updraft velocity
783 fluctuations is crucial to fully understand the drivers of droplet variability and the role of
784 aerosol as a driver of N_d variability.

785 Interestingly, we find that the same linear relationship between N_d^{lim} and σ_w that
786 describes the droplet formation during RACLETS holds for warm boundary layer clouds
787 formed in the SE US (Bougiatioti et al., 2020) and in the SE Atlantic (Kacarab et al., 2019).
788 This implies that the $N_d^{lim} \sim \sigma_w$ relationship may be universal, given the wide range of cloud
789 formation conditions it represents. If so, measurements (or remote sensing) of N_d and vertical
790 velocity distribution alone may be used to determine if cloud droplet formation is susceptible
791 to aerosol variations or solely driven by vertical velocity – without any additional aerosol
792 information.

793 Approaching velocity-limited conditions also carries important implications for ice-
794 formation processes in MPCs – as high N_d means that droplet size and the probability of riming
795 becomes minimum. Indeed, Lance et al. (2011) saw that the concentration of large droplets
796 exceeding $30 \mu\text{m}$ diameter – critical for rime splintering or droplet shattering to occur – drops
797 considerably for polluted Arctic MPCs with LWC $\sim 0.2 \text{ gm}^{-3}$ and $N_d \sim 300-400 \text{ cm}^{-3}$. Assuming

798 that these levels of N_d reflects N_d^{lim} , the corresponding σ_w is 0.3-0.35 ms^{-1} (Fig. 9), which is
799 characteristic for Arctic stratus. The same phenomenon can also occur in the Alpine clouds
800 studied here, given that velocity-limited conditions ($N_d/N_d^{lim} \geq 0.65$) occurs especially
801 during nighttime (Fig. 10). Therefore, observations of N_d and vertical velocity distribution (i.e.,
802 N_d^{lim}) may possibly be used to determine if SIP from riming and droplet shattering is impeded,
803 and if occurring frequently enough may help explain the existence of persistent MPCs.

804

805 **Data Availability:** The data used in this study can be downloaded from the EnviDat data portal
806 at <https://www.envidat.ch/group/about/raclets-field-campaign>. The meteorological
807 measurements are provided by the Swiss Federal Office of Meteorology and Climatology
808 MeteoSwiss at <https://gate.meteoswiss.ch/idaweb/login.do>. The Gaussian fits used for
809 determining σ_w and the droplet parameterization used for the calculations in the study are
810 available from athanasios.nenes@epfl.ch upon request.

811

812 **Author Contributions:** PG and AN designed and initiated the study with methodology and
813 software developed by AN. The analysis was carried out by PG and AN, with input from ABo,
814 JW, CM, ZAK, JH, MH, ABe, UL. CCN instrumentation was setup by ABo, aerosol
815 instrumentation and inlet setup were done by JW, CM and ZAK, cloud data by FR, JH, lidar
816 data by MH. Instrument maintenance during the field campaign was carried out by JW and
817 CM. Data curation was provided by PG, AN, JW, CM, FR. The original manuscript was written
818 by PG and AN with input from all authors. All authors reviewed and commented on the
819 manuscript.

820

821 **Funding:** This study was supported by the European Research Council, CoG-2016 project
822 PyroTRACH (726165) funded by H2020-EU.1.1. – Excellent Science, and from the European
823 Union Horizon 2020 project FORCeS under grant agreement No 821205. JW, FR, ZAK, JH,
824 UL acknowledge funding from the Swiss National Science Foundation (SNSF) grant number
825 200021_175824. CM acknowledges funding from the SNSF grant number 200021_169620.

826

827 **Conflicts of Interest:** The authors declare no conflict of interest.

828 **References**

- 829 Andreae, M. O. and Rosenfeld, D.: Aerosol-cloud-precipitation interactions. Part 1. The nature
830 and sources of cloud-active aerosols, *Earth-Science Rev.*, 89, 13–41,
831 doi:10.1016/j.earscirev.2008.03.001, 2008.
- 832 Baltensperger, U., Gäggeler, H. W., Jost, D. T., Lugauer, M., Schwikowski, M., Weingartner,
833 E. and Seibert, P.: Aerosol climatology at the high-alpine site Jungfraujoch, Switzerland,
834 *J. Geophys. Res.*, 102, 1997.
- 835 Barahona, D., West, R. E. L., Stier, P., Romakkaniemi, S., Kokkola, H. and Nenes, A.:
836 Comprehensively accounting for the effect of giant CCN in cloud activation
837 parameterizations, *Atmos. Chem. Phys.*, 10, 2467–2473, doi:10.5194/acp-10-2467-2010,
838 2010.
- 839 Barahona, D., Molod, A., Bacmeister, J., Nenes, A., Gettelman, A., Morrison, H., Phillips, V.,
840 and Eichmann, A.: Development of two-moment cloud microphysics for liquid and ice
841 within the NASA Goddard Earth Observing System Model (GEOS-5), *Geosci. Model
842 Dev.*, 7, 1733–1766, doi:10.5194/gmd-7-1733-2014, 2014.
- 843 Beck, A., Henneberger, J., Schöpfer, S., Fugal, J. and Lohmann, U.: HoloGondel: In situ cloud
844 observations on a cable car in the Swiss Alps using a holographic imager, *Atmos. Meas.
845 Tech.*, 10, 459–476, doi:10.5194/amt-10-459-2017, 2017.
- 846 Bergeron, T.: On the physics of clouds and precipitation, Report, *Int. Union Geod. Geophys.*,
847 doi:10.1038/174957a0, 1935.
- 848 Borys, R. D., Lowenthal, D. H., Cohn, S. A. and Brown, W. O. J.: Mountaintop and radar
849 measurements of anthropogenic aerosol effects on snow growth and snowfall rate,
850 *Geophys. Res. Lett.*, 30, doi:10.1029/2002gl016855, 2003.
- 851 Bougiatioti, A., Bezantakos, S., Stavroulas, I., Kalivitis, N., Kokkalis, P., Biskos, G.,
852 Mihalopoulos, N., Papayannis, A. and Nenes, A.: Biomass-burning impact on CCN
853 number, hygroscopicity and cloud formation during summertime in the eastern
854 Mediterranean, *Atmos. Chem. Phys.*, 16, 7389–7409, doi:10.5194/acp-16-7389-2016,
855 2016.
- 856 Bougiatioti, A., Nenes, A., Lin, J., Brock, C., de Gouw, J., Liao, J., Middlebrook, A. and Welti,
857 A.: Drivers of cloud droplet number variability in the summertime Southeast United States,
858 *Atmos. Chem. Phys.*, 20, doi:10.5194/acp-20-12163-2020, 2020.
- 859 Chow, F. K., De Wekker, Stephan, F. J. and Snyder, B. J.: Mountain weather research and
860 forecasting: recent progress and current challenges., Dordrecht: Springer, 2013. Internet
861 resource.

862 Conant, W. C., VanReken, T. M., Rissman, T. A., Varutbangkul, V., Jonsson, H. H., Nenes,
863 A., Jimenez, J. L., Delia, A. E., Bahreini, R., Roberts, G. C., Flagan, R. C., and Seinfeld,
864 J. H.: Aerosol-cloud drop concentration closure in warm cumulus, *J. Geophys. Res.-*
865 *Atmos.*, 109, D13204, doi:10.1029/2003JD004324, 2004.

866 Dusek, U., Frank, G. P., Curtius, J., Drewnick, F., Schneider, J., Krten, A., Rose, D., Andreae,
867 M. O., Borrmann, S. and Pöschl, U.: Enhanced organic mass fraction and decreased
868 hygroscopicity of cloud condensation nuclei (CCN) during new particle formation events,
869 *Geophys. Res. Lett.*, 37, L03804, doi:10.1029/2009GL040930, 2010.

870 Fanourgakis, G. S., Kanakidou, M., Nenes, A., Bauer, S. E., Bergman, T., Carslaw, K. S., Grini,
871 A., Hamilton, D. S., Johnson, J. S., Karydis, V. A., Kirkevåg, A., Kodros, J. K., Lohmann,
872 U., Luo, G., Makkonen, R., Matsui, H., Neubauer, D., Pierce, J. R., Schmale, J., Stier, P.,
873 Tsigaridis, K., van Noije, T., Wang, H., Watson-Parris, D., Westervelt, D. M., Yang, Y.,
874 Yoshioka, M., Daskalakis, N., Decesari, S., Gysel Beer, M., Kalivitis, N., Liu, X.,
875 Mahowald, N. M., Myriokefalitakis, S., Schrödner, R., Sfakianaki, M., Tsimpidi, A. P.,
876 Wu, M. and Yu, F.: Evaluation of global simulations of aerosol particle number and cloud
877 condensation nuclei, and implications for cloud droplet formation, *Atmos. Chem. Phys.*
878 *Discuss.*, 19, 8591–8617, doi:10.5194/acp-19-8591-2019, 2019.

879 Farrington, R. J., Connolly, P. J., Lloyd, G., Bower, K. N., Flynn, M. J., Gallagher, M. W.,
880 Field, P. R., Dearden, C. and Choulaton, T. W.: Comparing model and measured ice
881 crystal concentrations in orographic clouds during the INUPIAQ campaign, *Atmos. Chem.*
882 *Phys.*, 16, 4945–4966, doi:10.5194/acp-16-4945-2016, 2016.

883 Field, P. R., Lawson, R. P., Brown, P. R. A., Lloyd, G., Westbrook, C., Moisseev, D.,
884 Miltenberger, A., Nenes, A., Blyth, A., Choulaton, T., Connolly, P., Buehl, J., Crosier, J.,
885 Cui, Z., Dearden, C., DeMott, P., Flossmann, A., Heymsfield, A., Huang, Y., Kalesse, H.,
886 Kanji, Z. A., Korolev, A., Kirchgaessner, A., Lasher-Trapp, S., Leisner, T., McFarquhar,
887 G., Phillips, V., Stith, J. and Sullivan, S.: Chapter 7. Secondary Ice Production - current
888 state of the science and recommendations for the future, *Meteorol. Monogr.*,
889 doi:10.1175/amsmonographs-d-16-0014.1, 2017.

890 Findeisen, W.: Die kolloidmeteorologischen vorgänge bei der niederschlagsbildung, *Meteorol.*
891 *Zeitschrift*, 55, 121–133, 1938.

892 Fountoukis, C. and Nenes, A.: Continued development of a cloud droplet formation
893 parameterization for global climate models, *J. Geophys. Res.*, 110, D1121,
894 doi:10.1029/2004JD005591, 2005.

895 Fountoukis, C., Nenes, A., Meskhidze, N., Bahreini, R., Conant, W. C., Jonsson, H., Murphy,

896 S., Sorooshian, A., Varutbangkul, V., Brechtel, F., Flagan, R. C. and Seinfeld, J. H.:
897 Aerosol-cloud drop concentration closure for clouds sampled during the International
898 Consortium for Atmospheric Research on Transport and Transformation 2004 campaign,
899 *J. Geophys. Res.*, 112, doi:10.1029/2006JD007272, 2007.

900 Fugal, J. P., Schulz, T. J. and Shaw, R. A.: Practical methods for automated reconstruction and
901 characterization of particles in digital in-line holograms, *Meas. Sci. Technol.*, 20,
902 doi:10.1088/0957-0233/20/7/075501, 2009.

903 Ghan, S., Guzman, G., and Abdul-Razzak, H.: Competition between sea salt and sulfate
904 particles as cloud condensation nuclei, *J. Atmos. Sci.*, 55, 3340–3347, 1998.

905 Ghan, S.J., Abdul-Razzak, H., Nenes, A., Ming, Y., Liu, X., Ovchinnikov, M., Shipway, B.,
906 Meskhidze, N., Xu, J. and Shi, X.: Droplet Nucleation: Physically-based Parameterization
907 and Comparative Evaluation, *J. Adv. Model. Earth Syst.*, 3, doi:10.1029/2011MS000074,
908 2011.

909 Griesche, H. J., Seifert, P., Ansmann, A., Baars, H., Barrientos Velasco, C., Bühl, J.,
910 Engelmann, R., Radenz, M. and Zhenping, Y.: Application of the shipborne remote
911 sensing supersite OCEANET for profiling of Arctic aerosols and clouds during Polarstern
912 cruise PS106, *Atmos. Meas. Tech. Discuss.*, 1–37, doi:10.5194/amt-2019-434, 2019.

913 Grosvenor, D. P., Sourdeval, O., Zuidema, P., Ackerman, A., Alexandrov, M. D., Bennartz,
914 R., Boers, R., Cairns, B., Chiu, J. C., Christensen, M., Deneke, H., Diamond, M., Feingold,
915 G., Fridlind, A., Hünerbein, A., Knist, C., Kollias, P., Marshak, A., McCoy, D., Merk, D.,
916 Painemal, D., Rausch, J., Rosenfeld, J., Russchenberg, H., Seifert, P., Sinclair, K., Stier,
917 P., van Diedenhoven, B., Wendisch, M., Werner, F., Wood, R., Zhang, Z. and Quaas, J.:
918 Remote sensing of droplet number concentration in warm clouds: A review of the current
919 state of knowledge and perspectives. *Reviews of Geophysics*, 56, 409–453.
920 doi:10.1029/2017RG000593, 2018.

921 Grubisic, V. and Billings, B. J.: Climatology of the Sierra Nevada mountain-wave events, *Mon.*
922 *Weather Rev.*, 136, 757–768, doi:10.1175/2007MWR1902.1, 2008.

923 Hammer, E., Bukowiecki, N., Gysel, M., Jurányi, Z., Hoyle, C. R., Vogt, R., Baltensperger, U.
924 and Weingartner, E.: Investigation of the effective peak supersaturation for liquid-phase
925 clouds at the high-alpine site Jungfraujoch, Switzerland (3580 m a.s.l.), *Atmos. Chem.*
926 *Phys.*, 14, 1123–1139, doi:10.5194/acp-14-1123-2014, 2014.

927 Hammer, E., Bukowiecki, N., Luo, B. P., Lohmann, U., Marcolli, C., Weingartner, E.,
928 Baltensperger, U. and Hoyle, C. R.: Sensitivity estimations for cloud droplet formation in
929 the vicinity of the high-alpine research station Jungfraujoch (3580 m a.s.l.), *Atmos. Chem.*

930 Phys., 15, 10309–10323, doi:10.5194/acp-15-10309-2015, 2015.

931 Henneberg, O., Henneberger, J. and Lohmann, U.: Formation and development of orographic
932 mixed-phase clouds, *J. Atmos. Sci.*, 74, 3703–3724, doi:10.1175/JAS-D-16-0348.1, 2017.

933 Henneberger, J., Fugal, J. P., Stetzer, O. and Lohmann, U.: HOLIMO II: A digital holographic
934 instrument for ground-based in situ observations of microphysical properties of mixed-
935 phase clouds, *Atmos. Meas. Tech.*, 6, 2975–2987, doi:10.5194/amt-6-2975-2013, 2013.

936 Herrmann, E., Weingartner, E., Henne, S., Vuilleumier, L., Bukowiecki, N., Steinbacher, M.,
937 Conen, F., Collaud Coen, M., Hammer, E., Jurányi, Z., Baltensperger, U. and Gysel, M.:
938 Analysis of long-term aerosol size distribution data from Jungfraujoch with emphasis on
939 free tropospheric conditions, cloud influence, and air mass transport, *J. Geophys. Res.*
940 *Atmos.*, 120, 9459–9480, doi:10.1002/2015JD023660, 2015.

941 Hoyle, C. R., Webster, C. S., Rieder, H. E., Nenes, A., Hammer, E., Herrmann, E., Gysel, M.,
942 Bukowiecki, N., Weingartner, E., Steinbacher, M. and Baltensperger, U.: Chemical and
943 physical influences on aerosol activation in liquid clouds : a study based on observations
944 from the Jungfraujoch , Switzerland, *Atmos. Chem. Phys.*, 16, 4043–4061,
945 doi:10.5194/acp-16-4043-2016, 2016.

946 IPCC: Climate Change 2013: The Physical Science Basis. Contribution of Working Group I to
947 the Fifth Assessment Report of the Intergovernmental Panel on Climate Change, edited
948 by: Stocker, T. F., Qin, D., Plattner, G.-K., Tignor, M., Allen, S. K., Boschung, Cambridge
949 Univ. Press. Cambridge, UK New York, NY, USA, 1535 pp.,
950 doi:10.1017/CBO9781107415324, 2013.

951 Jensen, J. B. and Charlson R. J.: On the efficiency of nucleation scavenging, *Tellus*, 36B, 367–
952 375, doi: 10.3402/tellusb.v36i5.14917, 1984.

953 Jurányi, Z., Gysel, M., Weingartner, E., Decarlo, P. F., Kammermann, L. and Baltensperger,
954 U.: Measured and modelled cloud condensation nuclei number concentration at the high
955 alpine site Jungfraujoch, *Atmos. Chem. Phys.*, 10, 7891–7906, doi:10.5194/acp-10-7891-
956 2010, 2010.

957 Jurányi, Z., Gysel, M., Weingartner, E., Bukowiecki, N., Kammermann, L. and Baltensperger,
958 U.: A 17 month climatology of the cloud condensation nuclei number concentration at the
959 high alpine site Jungfraujoch, *J. Geophys. Res.*, 116, D1020, doi:10.1029/2010JD015199,
960 2011.

961 Kacarab, M., Lee Thornhill, K., Dobracki, A., Howell, S. G., O'Brien, J. R., Freitag, S., Poellot,
962 M. R., Wood, R., Zuidema, P., Redemann, J. and Nenes, A.: Biomass burning aerosol as
963 a modulator of the droplet number in the southeast Atlantic region, *Atmos. Chem. Phys.*,

964 20, 3029–3040, doi:10.5194/acp-20-3029-2020, 2020.

965 Kalkavouras, P., Bougiatioti, A., Kalivitis, N., Stavroulas, I., Tombrou, M., Nenes, A. and
966 Mihalopoulos, N.: Regional new particle formation as modulators of cloud condensation
967 nuclei and cloud droplet number in the eastern Mediterranean, *Atmos. Chem. Phys.*, 19,
968 6185–6203, doi:10.5194/acp-19-6185-2019, 2019.

969 Kammermann, L., Gysel, M., Weingartner, E. and Baltensperger, U.: 13-month climatology of
970 the aerosol hygroscopicity at the free tropospheric site Jungfraujoch (3580 m a.s.l.),
971 *Atmos. Chem. Phys.*, 10, doi:10.5194/acp-10-10717-2010, 2010.

972 Kleissl, J., Honrath, R. E., Dziobak, M. P., Tanner, D., Val Martín, M., Owen, R. C. and
973 Helmig, D.: Occurrence of upslope flows at the Pico mountaintop observatory: A case
974 study of orographic flows on a small, volcanic island, *J. Geophys. Res. Atmos.*, 112,
975 D10S3, doi:10.1029/2006JD007565, 2007.

976 Korolev, A. and Isaac, G.: Phase transformation of mixed-phase clouds, *Q. J. R. Meteorol.*
977 *Soc.*, 129, 19–38, doi:10.1256/qj.01.203, 2003.

978 Lance, S., Shupe, M. D., Feingold, G., Brock, C. A., Cozic, J., Holloway, J. S., Moore, R. H.,
979 Nenes, A., Schwarz, J. P., Spackman, J. R., Froyd, K. D., Murphy, D. M., Brioude, J.,
980 Cooper, O. R., Stohl, A. and Burkhardt, J. F.: Cloud condensation nuclei as a modulator of
981 ice processes in Arctic mixed-phase clouds, *Atmos. Chem. Phys.*, 11, 8003–8015,
982 doi:10.5194/acp-11-8003-2011, 2011.

983 Lanz, V. A., Prévôt, A. S. H., Alfarra, M. R., Weimer, S., Mohr, C., Decarlo, P. F., Gianini, M.
984 F. D., Hueglin, C., Schneider, J., Favez, O., D’Anna, B., George, C. and Baltensperger,
985 U.: Characterization of aerosol chemical composition with aerosol mass spectrometry in
986 Central Europe: An overview, *Atmos. Chem. Phys.*, 10, 10453–10471, doi:10.5194/acp-
987 10-10453-2010, 2010.

988 Latham, T. L., Beyersdorf, A. J., Thornhill, K. L., Winstead, E. L., Cubison, M. J., Hecobian,
989 A., Jimenez, J. L., Weber, R. J., Anderson, B. E. and Nenes, A.: Analysis of CCN activity
990 of Arctic aerosol and Canadian biomass burning during summer 2008, *Atmos. Chem.*
991 *Phys.*, 13, 2735–2756, doi:10.5194/acp-13-2735-2013, 2013.

992 Lauber, A., Henneberger, J., Mignani, C., Ramelli, F., Pasquier, J. T., Wieder, J., Hervo, M.
993 and Lohmann, U.: Continuous secondary-ice production initiated by updrafts through the
994 melting layer in mountainous regions, 2020*Atmos. Chem. Phys.*, 21, 3855–3870,
995 doi:10.5194/acp-21-3855-2021, 2021.

996 Lloyd, G., Choularton, T. W., Bower, K. N., Gallagher, M. W., Connolly, P. J., Flynn, M.,
997 Farrington, R., Crosier, J., Schlenzcek, O., Fugal, J. and Henneberger, J.: The origins of

998 ice crystals measured in mixed-phase clouds at the high-alpine site Jungfraujoch, Atmos.
999 Chem. Phys., 15, 12953–12969, doi:10.5194/acp-15-12953-2015, 2015.

1000 Lohmann, U.: A glaciation indirect aerosol effect caused by soot aerosols, Geophys. Res. Lett.,
1001 29(4), doi:10.1029/2001GL014357, 2002.

1002 Lohmann, U. and Feichter, J.: Global indirect aerosol effects: a review, Atmos. Chem. Phys.,
1003 5, 715–737, doi:10.5194/acp-5-715-2005, 2005.

1004 Lohmann, U., Henneberger, J., Henneberg, O., Fugal, J. P., Bühl, J. and Kanji, Z. A.:
1005 Persistence of orographic mixed-phase clouds, Geophys. Res. Lett., 43, 10512–10519,
1006 doi:10.1002/2016GL071036, 2016.

1007 Lohmann, U.: Anthropogenic Aerosol Influences on Mixed-Phase Clouds, Curr. Clim. Chang.
1008 Reports, 3, 32–44, doi:10.1007/s40641-017-0059-9, 2017.

1009 Meskhidze, N., Nenes, A., Conant, W. C. and Seinfeld, J. H.: Evaluation of a new cloud droplet
1010 activation parameterization with in situ data from CRYSTAL-FACE and CSTRIFE, J.
1011 Geophys. Res., 110, D1620, doi:10.1029/2004JD005703, 2005.

1012 Mignani, C., Creamean, J. M., Zimmermann, L., Alewell, C., and Conen, F.: New type of
1013 evidence for secondary ice formation at around $-15\text{ }^{\circ}\text{C}$ in mixed-phase clouds, Atmos.
1014 Chem. Phys., 19, 877–886, doi:10.5194/acp-19-877-2019, 2019.

1015 Mignani, C., Wieder, J., Sprenger, M. A., Kanji, Z. A., Henneberger, J., Alewell, C. and Conen,
1016 F.: Towards parameterising atmospheric concentrations of ice-nucleating particles active
1017 at moderate supercooling, Atmos. Chem. Phys., 21, 657–664, doi:10.5194/acp-21-657-
1018 2021, 2021.

1019 Moore, R. H., Bahreini, R., Brock, C. A., Froyd, K. D., Cozic, J., Holloway, J. S., Middlebrook,
1020 A. M., Murphy, D. M. and Nenes, A.: Hygroscopicity and composition of Alaskan Arctic
1021 CCN during April 2008, Atmos. Chem. Phys., 11, 11807–11825, doi:10.5194/acp-11-
1022 11807-2011, 2011.

1023 Morales Betancourt, R. and Nenes, A.: Characteristic updrafts for computing distribution-
1024 averaged cloud droplet number and stratocumulus cloud properties, J. Geophys. Res., 115,
1025 D1822, doi:10.1029/2009JD013233, 2010.

1026 Morales Betancourt, R., Nenes, A., Jonsson, H., Flagan, R. C. and Seinfeld, J. H.: Evaluation
1027 of an entraining droplet activation parameterization using in situ cloud data, J. Geophys.
1028 Res., 116, D1520, doi:10.1029/2010JD015324, 2011.

1029 Morales Betancourt, R., and Nenes, A.: Aerosol Activation Parameterization: The population
1030 splitting concept revisited, Geosci.Mod.Dev., 7, 2345–2357, doi:10.5194/gmd-7-2345-
1031 2014, 2014.

1032 Mosimann, L, Weingartner, E. and Waldvogel A.: An analysis of accreted drop sizes and mass
1033 on rimed snow crystals., *J. Atmos. Sci.*, 51, 1548–1558, 1994.

1034 Muhlbauer, A. and Lohmann, U.: Sensitivity studies of aerosol-cloud interactions in mixed-
1035 phase orographic precipitation, *J. Atmos. Sci.*, 66, 2517–2538,
1036 doi:10.1175/2009JAS3001.1, 2009.

1037 Nenes, A., Ghan, S., Abdul-Razzak, H., Chuang, P.Y., Seinfeld, J.H.: Kinetic Limitations on
1038 Cloud Droplet Formation and Impact on Cloud Albedo, *Tellus*, 53B, 133-149, 2001.

1039 Nenes, A. and Seinfeld, J. H.: Parameterization of cloud droplet formation in global climate
1040 models, *J. Geophys. Res.*, 108, 4415, doi:10.1029/2002jd002911, 2003.

1041 Okamoto, S. and Tanimoto, H.: A review of atmospheric chemistry observations at mountain
1042 sites, *Prog. Earth Planet. Sci.*, 3, 34, doi:10.1186/s40645-016-0109-2, 2016.

1043 Petters, M. D. and Kreidenweis, S. M.: A single parameter representation of hygroscopic
1044 growth and cloud condensation nucleus activity, *Atmos. Chem. Phys.*, 7, 1961–1971,
1045 doi:10.5194/acp-7-1961-2007, 2007.

1046 Pringle, K. J., Tost, H., Pozzer, A., Pöschl, U. and Lelieveld, J.: Global distribution of the
1047 effective aerosol hygroscopicity parameter for CCN activation, *Atmos. Chem. Phys.*, 10,
1048 5241–5255, doi:10.5194/acp-10-5241-2010, 2010.

1049 Pruppacher, H. R. and Klett, J. D.: *Microphysics of Clouds and Precipitation*, 2nd ed., 1997.

1050 Ramelli, F., Beck, A., Henneberger, J. and Lohmann, U.: Using a holographic imager on a
1051 tethered balloon system for microphysical observations of boundary layer clouds, *Atmos.*
1052 *Meas. Tech.*, 13, 925–939, doi:10.5194/amt-13-925-2020, ~~2020a~~2020.

1053 Ramelli, F., Henneberger, J., David, R. O., Lauber, A., Pasquier, J. T., Wieder, J., Bühl, J.,
1054 Seifert, P., Engelmann, R., Hervo, M. and Lohmann, U.: Influence of low-level blocking
1055 and turbulence on the microphysics of a mixed-phase cloud in an inner-Alpine valley,
1056 *Atmos. Chem. Phys. Discuss.*, 21, 5151–5172, doi:10.5194/acp-2020-774, ~~in review,~~
1057 ~~2020b~~21-5151-2021, 2021a.

1058 Ramelli, F., Henneberger, J., David, R. O., Bühl, J., Radenz, M., Seifert, P., Wieder, J., Lauber,
1059 A., Pasquier, J. T., Engelmann, R., Mignani, C., Hervo, M. and Lohmann, U.:
1060 Microphysical investigation of the seeder and feeder region of an Alpine mixed-phase
1061 cloud, ~~submitted manuscript, 2020e.~~*Atmos. Chem. Phys.*, 21, 6681–6706,
1062 doi:10.5194/acp-21-6681-2021, 2021b.

1063 Reutter, P., Su, H., Trentmann, J., Simmel, M., Rose, D., Gunthe, S. S., Wernli, H., Andreae,
1064 M. O. and Pöschl, U.: Aerosol- and updraft-limited regimes of cloud droplet formation:
1065 Influence of particle number, size and hygroscopicity on the activation of cloud

1066 condensation nuclei (CCN), *Atmos. Chem. Phys.*, 9, 7067–7080, doi:10.5194/acp-9-7067-
1067 2009, 2009.

1068 Roberts, G. C. and Nenes, A.: A continuous-flow streamwise thermal-gradient CCN chamber
1069 for atmospheric measurements, *Aerosol Sci. Technol.*, 39(3), 206–221,
1070 doi:10.1080/027868290913988, 2005.

1071 Roe, G. H.: Orographic Precipitation, *Annu. Rev. Earth Planet. Sci.*, 33, 645–671,
1072 doi:10.1146/annurev.earth.33.092203.122541, 2005.

1073 Rose, D., Gunthe, S. S., Mikhailov, E., Frank, G. P., Dusek, U., Andreae, M. O. and Pöschl,
1074 U.: Calibration and measurement uncertainties of a continuous-flow cloud condensation
1075 nuclei counter (DMT-CCNC): CCN activation of ammonium sulfate and sodium chloride
1076 aerosol particles in theory and experiment, *Atmos. Chem. Phys.*, 8(5), 1153–1179,
1077 doi:10.5194/acp-8-1153-2008, 2008.

1078 Rotunno, R. and Houze, R. A.: Lessons on orographic precipitation from the Mesoscale Alpine
1079 Programme, *Q. J. R. Meteorol. Soc.*, 133, 811–830, doi:10.1002/qj.67, 2007.

1080 Saleeby, S. M., Cotton, W. R., Lowenthal, D. and Messina, J.: Aerosol impacts on the
1081 microphysical growth processes of orographic snowfall, *J. Appl. Meteorol. Climatol.*, 52,
1082 834–852, doi:10.1175/JAMC-D-12-0193.1, 2013.

1083 Seinfeld, J. H. and Pandis, S. N.: *Atmospheric Chemistry and Physics: From Air Pollution to*
1084 *Climate Change*, 2nd Edn., John Wiley, edited by: Hoboken, N. J., 2006.

1085 Seinfeld, J. H., Bretherton, C., Carslaw, K. S., Coe, H., DeMott, P. J., Dunlea, E. J., Feingold,
1086 G., Ghan, S., Guenther, A. B., Kahn, R., Kraucunas, I., Kreidenweis, S. M., Molina, M. J.,
1087 Nenes, A., Penner, J. E., Prather, K. A., Ramanathan, V., Ramaswamy, V., Rasch, P. J.,
1088 Ravishankara, A. R., Rosenfeld, D., Stephens, G. and Wood, R.: Improving our
1089 fundamental understanding of the role of aerosol-cloud interactions in the climate system,
1090 *Proc. Natl. Acad. Sci. U. S. A.*, 113, 5781–5790, doi:10.1073/pnas.1514043113, 2016.

1091 Smith, R. B.: Progress on the theory of orographic precipitation, *Spec. Pap. Geol. Soc. Am.*,
1092 398, 1–16, doi:10.1130/2006.2398(01), 2006.

1093 Snider, J. R., Leon, D. and Wang, Z.: Droplet concentration and spectral broadening in
1094 Southeast Pacific stratocumulus clouds, *J. Atmos. Sci.*, 74(3), 719–749. doi:10.1175/JAS-
1095 D-16-0043.1, 2017.

1096 Sotiropoulou, G., Sullivan, S., Savre, J., Lloyd, G., Lachlan-Cope, T., Ekman, A. M. L. and
1097 Nenes, A.: The impact of secondary ice production on Arctic stratocumulus, *Atmos. Chem.*
1098 *Phys.*, 20, 1301–1316, doi:10.5194/acp-20-1301-2020, 2020.

1099 Sotiropoulou, G., Vignon, É., Young, G., Morrison, H., O'Shea, S. J., Lachlan-Cope, T., Berne,

1100 A., and Nenes, A.: Secondary ice production in summer clouds over the Antarctic coast:
1101 an underappreciated process in atmospheric models, *Atmos. Chem. Phys.*, 21, 755–771,
1102 <https://doi.org/10.5194/acp-21-755-2021>, 2021.

1103 Sud, Y.C, Lee, D., Oreopoulos, L., Barahona, D., Nenes, A. and M.J. Suarez: Performance of
1104 McRAS-AC in the GEOS-5 AGCM: aerosol-cloud-microphysics, precipitation, cloud
1105 radiative effects, and circulation, *Geosci. Model. Dev.*, 6, 57–79, doi:10.5194/gmd-6-57-
1106 2013, 2013.

1107 Sullivan, S. C., Lee, D., Oreopoulos, L. and Nenes, A.: Role of updraft velocity in temporal
1108 variability of global cloud hydrometeor number, *Proc. Natl. Acad. Sci. U. S. A.*, 113,
1109 5791–5796, doi:10.1073/pnas.1514039113, 2016.

1110 Sullivan, S. C., Barthlott, C., Crosier, J., Zhukov, I., Nenes, A. and Hoose, C.: The effect of
1111 secondary ice production parameterization on the simulation of a cold frontal rainband,
1112 *Atmos. Chem. Phys.*, 18, 16461–16480, doi:10.5194/acp-18-16461-2018, 2018.

1113 Tokay, A., Wolff, D. B. and Petersen, W. A.: Evaluation of the new version of the laser-optical
1114 disdrometer, OTT parsivel, *J. Atmos. Ocean. Technol.*, 31(6), 1276–1288,
1115 doi:10.1175/JTECH-D-13-00174.1, 2014.

1116 Touloupas, G., Lauber, A., Henneberger, J., Beck, A. and Lucchi, A.: A convolutional neural
1117 network for classifying cloud particles recorded by imaging probes, *Atmos. Meas. Tech.*,
1118 13(5), 2219–2239, doi:10.5194/amt-13-2219-2020, 2020.

1119 Tröstl, J., Herrmann, E., Frege, C., Bianchi, F., Molteni, U., Bukowiecki, N., Hoyle, C. R.,
1120 Steinbacher, M., Weingartner, E., Dommen, J., Gysel, M. and Baltensperger, U.:
1121 Contribution of new particle formation to the total aerosol concentration at the high-
1122 altitude site Jungfraujoch (3580masl, Switzerland), *J. Geophys. Res. Atmos.*, 121, 11692–
1123 11711, doi:10.1002/2015JD024637, 2016.

1124 Twomey, S., Radiative properties of clouds, pp. 278 – 280, in *Aerosol Effects on Climate*, S.G.
1125 Jennings Editor, The University of Arizona Press, Tucson, 1993.

1126 Vosper, S. B., Wells, H., Sinclair, J. A. and Sheridan, P. F.: A climatology of lee waves over
1127 the UK derived from model forecasts, *Meteorol. Appl.*, 20, 466–481,
1128 doi:10.1002/met.1311, 2013.

1129 Wang, J., Lee, Y. N., Daum, P. H., Jayne, J. and Alexander, M. L.: Effects of aerosol organics
1130 on cloud condensation nucleus (CCN) concentration and first indirect aerosol effect,
1131 *Atmos. Chem. Phys.*, 8, 6325–6339, doi:10.5194/acp-8-6325-2008, 2008.

1132 Wegener, A.: *Thermodynamik der Atmosphäre*, Ger. Barth, Leipzig, 331 pp., 1911.

1133 Zubler, E. M., Lohmann, U., Lüthi, D., Schär, C. and Muhlbauer, A.: Statistical analysis of

1134 aerosol effects on simulated mixed-phase clouds and precipitation in the Alps, J. Atmos.
1135 Sci., 68, 1474–1492, doi:10.1175/2011JAS3632.1, 2011-
1136 .

Formatted: Indent: Left: 0", Hanging: 0.3", No widow/orphan control, Don't adjust space between Latin and Asian text, Don't adjust space between Asian text and numbers